Calibration of a glueing robot for assembly of the P2 tracking detector

by

Patrick Riederer

Bachelor thesis in physics
submitted to Fachbereich Physik, Mathematik und Informatik (FB 08)
at Johannes-Gutenberg University Mainz
5^{th} August 2021

1^{st} referee: Prof. Dr. Niklaus Berger
2^{nd} referee: Prof. Dr. Lucia Masetti

I hereby confirm that I have written the following thesis by myself without any other contributors or sources than cited.

Patrick Riederer

Mainz, 5$^{\text{th}}$ August 2021

Patrick Riederer
AG Berger
Institute for Nuclear Physics
Staudingerweg 9
Johannes Gutenberg-Universität D-55099 Mainz
priedere@students.uni-mainz.de

Abstract

The Mainz Energy recovery Superconducting Accelerator (MESA) will offer an intense electron beam for nuclear physics experiments such as P2. The tracking detector of P2 consists of 4320 High Voltage Monolithic Active Pixel Sensors (HV-MAPS) glued onto 464 polyamide strips which are manufactured semi-automatically using a four axis glueing robot.
Within this thesis the three linear axes have been put into service as well as initial internal parameters investigated and defined. For bed-leveling two methods were developed and their results analysed. However, there is the need of a more reliable approach to confirm data gained. Furthermore, the perpendicularity of two axes was investigated and assured within an angle error in $\mathcal{O}(10'')$.
The jet dispenser used to apply the glue was set up and a method developed to quantitatively analyse the dispensed glue dots. Two single component epoxy resins (*Strucalit® 3060 N* and *DYMAX® Multi-Cure® 6-621*) were tested and ideal dispensing parameters established.

Kurzfassung

Der Teilchenbeschleuniger MESA (Mainzer Energy recovery Superconducting Accelerator) wird einen hochenergetischen Elektronenstrahl für kernphysikalische Experimente wie P2 bereitstellen. Der Spurdetektor von P2 besteht aus 4320 HV-MAPS (High Voltage Monolithic Active Pixel Sensors), die auf 464 Kaptonstreifen geklebt werden. Letztere werden halbautomatisch mit einem vierachsigen Kleberoboter hergestellt.
Im Rahmen dieser Bachelorarbeit wurden die drei Linearachsen des Roboters in Betrieb genommen sowie interne Parameter untersucht und definiert. Für die Nivellierung des Arbeitsbereichs wurden zwei Messmethoden entwickelt und deren Ergebnisse analysiert. Es besteht jedoch die Notwendigkeit eines zuverlässigeren Ansatzes zur Bestätigung der gewonnenen Daten. Außerdem wurde die Rechtwinkligkeit zweier Achsen untersucht und bezüglich eines Fehlers in $\mathcal{O}(10'')$ sichergestellt.
Der zum Auftragen des Klebstoffs verwendete Jet-Dispenser wurde final eingebaut und eine Methode zur quantitativen Analyse von dispensierten Klebstofftropfen entwickelt. Zwei einkomponentige Epoxidharze (*Strucalit® 3060 N* und *DYMAX® Multi-Cure® 6-621*) wurden getestet und die idealen Dosierparameter ermittelt.

Contents

Contents 4

1. Introduction 5

2. Setup 7
- 2.1. General setup . . . 7
- 2.2. Axis . . . 9
- 2.3. Jet dispenser and pneumatic system . . . 14

3. Initial operation 16
- 3.1. Axis . . . 16
  - 3.1.1. Interface . . . 16
  - 3.1.2. Establish operative condition . . . 16
- 3.2. Weight compensation . . . 20
  - 3.2.1. General description . . . 20
  - 3.2.2. Pressure adjustment . . . 20
- 3.3. Jet dispenser . . . 25
  - 3.3.1. General description . . . 25
  - 3.3.2. Parameter adjustment . . . 26

4. Precision measurements and calibration 31
- 4.1. Flatness of the granite slab . . . 31
  - 4.1.1. Method 1 - usage of *Drive I_Force* . . . 31
  - 4.1.2. Method 2 - usage of an indicator . . . 37
  - 4.1.3. Comparison and outlook . . . 41
- 4.2. Perpendicularity x-y-axes . . . 42

List of Figures 46

List of Tables 47

Bibliography 49

A. Screenshots WebMotion® web interface 50

B. Axes parameters 53

C. Evaluation standards glue dots 55

D. Statistics on dispensing parameters 57

E. Position per force 60

F. Acknowledgements 62

1. Introduction

Currently the Standard Model of Particle Physics (SM) is the best and the generally accepted description of matter, predicting high accuracy experiments in particle physics down to a scale of 1×10^{-19} m. However, neither the matter-antimatter asymmetry of the universe nor finite neutrino masses as well as further anomalies are explained by the SM. The search for New Physics beyond the SM is therefore considered to be one of the main challenges of modern particle physics and experimental research is being undertaken with various high precision experiments throughout the world.

The Mainz Energy recovery Superconducting Accelerator (MESA) - still under construction - will offer an intense electron beam of 150 µA at an energy of 155 MeV [1]. Two experimental facilities are planned, the MAGIX experiment with multiple purposes in nucleon and nuclear physics as well as the P2 experiment whose main purpose is to measure the proton weak charge and from this the weak mixing angle (Weinberg-angle) with a relative uncertainty of 0.15 % [1].
Elastic electron-proton scattering (as observed in the P2 experiment) violates parity. The resulting (small) asymmetry can be used to calculate the weak proton charge which is highly sensitive to the weak mixing angle θ_W (often $s_W^2 \coloneqq \sin^2\theta_W$) [1]. A precise determination of the weak proton charge will therefore also result in precise measurement of s_W^2.

The P2 experiment (see figure 1.1) consists of a liquid hydrogen target, hit by the polarised electron beam whose polarization is switched at kHz rate. The scattered electrons are separated according to their momentum by the 0.6 T magnetic field before entering the tracking detector for path and thereby momentum transfer determination. A circular integrating Cherenkov detector is placed thereafter to detect the (very small - P2 has to run for about 11 000 h to achieve the desired accuracy) cross-section asymmetry.

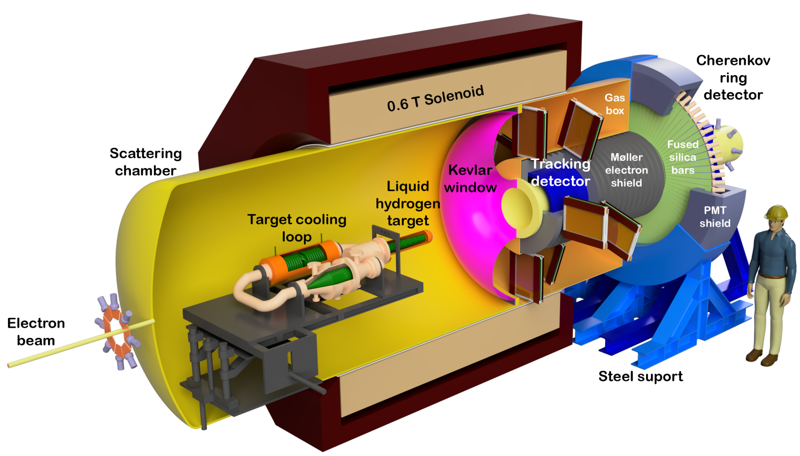

Figure 1.1.: Setup of the P2 experiment [8].

Because the tracking detector has to be placed inside the solenoid, Bremsstrahlung photons may affect the detector. To minimise this effect, the material budget must be kept as low as possible to limit photon interactions. Furthermore, low momenta of the scattered electrons make a long drift region without matter necessary. The detector therefore consists of two double detector planes as shown in figure 1.2a. Each plane covers only about 15 deg of the azimuthal angle whereby it is planned to use eight double segments in total to cover up and down as well as left and right asymmetries [1]. The track of a particle (and therefore its momentum) can then be reconstructed from the four points where it hit the detector.
The actual hits are detected by High Voltage Monolithic Active Pixel Sensors (HV-MAPS) [14], which require supply voltages, a data readout and a support structure to hold them in place as well as allowing efficient cooling with gaseous helium (helium is chosen in favour of any other gas to keep the material budget low). To meet these requirements, the HV-MAPS are to be glued on polyimide strips which in turn are mounted on a Printed Circuit Board (PCB) on each side. To add rigidity to these strips and allow for a well defined laminar helium flow right beneath them, two additional polyimide strips in a v-shape (so called v-folds) are glued onto the first [14]. This internal setup of each strip module is shown in figure 1.2b where the supporting PCBs are shown in green, the HV-MAPS in dark grey with a red line and any polyamide structure in orange.
To glue everything together, a radiation hard and both in amount as well as location precisely applicable glue needs to be used. Because it has been used with good results in other detectors an epoxy resin of the Araldite® family is thought to be suitable to glue the HV-MAPS as well as v-folds onto the polyamide strips. But also singe component epoxy resins are taken into consideration. A total of 416 strips are needed for the P2 experiment, so a mechanised, easy to use and especially precise solution for mass manufacturing is required. It was decided to build a robot from linear and rotary axes made by the Swiss manufacturer Jenny Science AG to make this possible. This thesis deals with the initial operation of the glueing robot, its testing and calibration phase as well as glue tests on different epoxy resins.

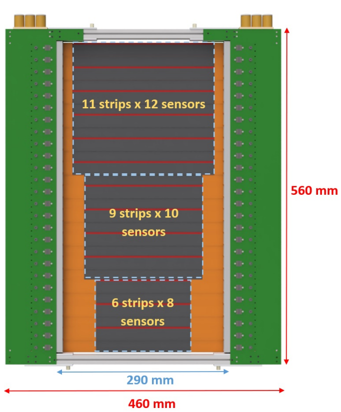

(a) Top view of a strip module [8].

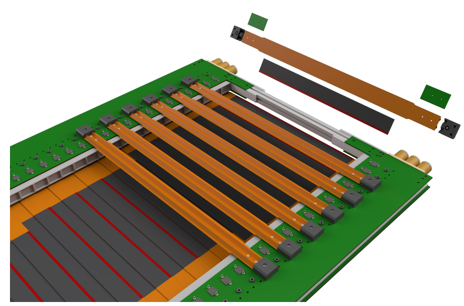

(b) Schematic figure of a strip module with the lower half fully and the upper partially assembled. All parts of a strip submodule are shown on the upper right [8].

Figure 1.2.: Strip module of the tracking detector. The detector is built from eight strip modules, each consisting of two layers with 26 strips. The PCBs (green) act as a support structure containing electronic and cooling infrastructure. HV-MAPS (dark grey with red line) are held in place by kapton strips (orange).

2. Setup

In this chapter the general setup of the hardware is explained. A general overview is provided by section 2.1, detailed information about individual components are given in section 2.2 for the axes and in section 2.3 for the glue jet dispension system.

2.1. General setup

The glueing robot, shown in figure 2.2, is a small (50 cm × 50 cm × 200 cm in total) and portable apparatus made of aluminium extrusions mounted on four lockable wheels with a computer monitor hanging above the main structure. A 5 cm thick and 40 cm wide (x- and y-direction) granite slab with a defined flatness of less than 2 µm deviation from the mean serves as a working surface. Nine M8 threads with a depth of 33 mm are embedded to fixate any tools. The threads are placed in a 15 cm grid with 5 cm distance to the edge of the granite slab. The movable parts consist of four axes (x, y, z and r) made by the Swiss manufacturer Jenny Science AG.

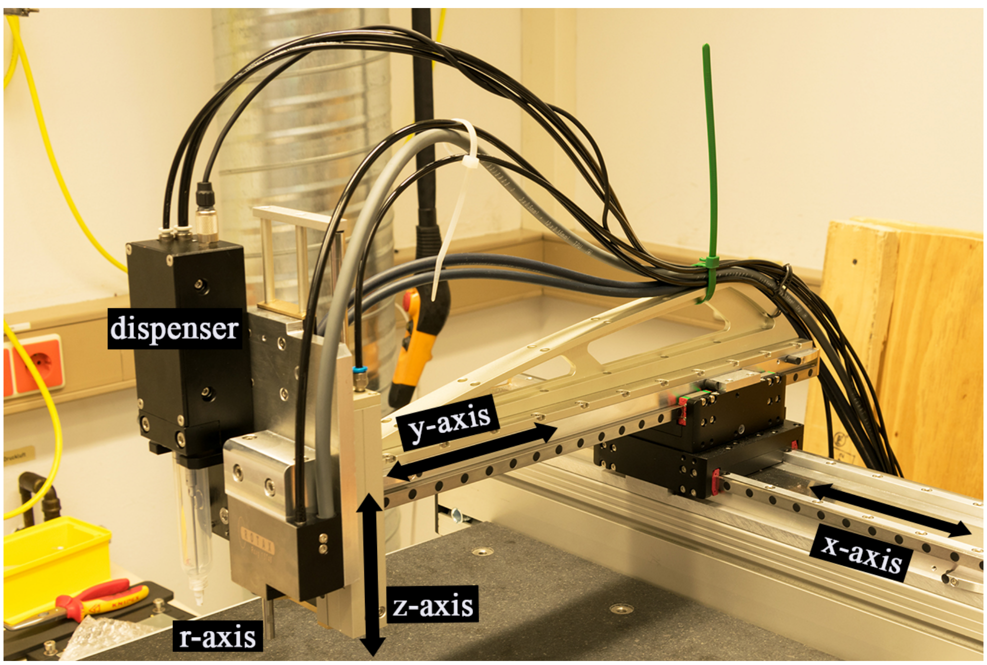

Figure 2.1.: Close-up of the working surface with all four axes and the glue dispenser.

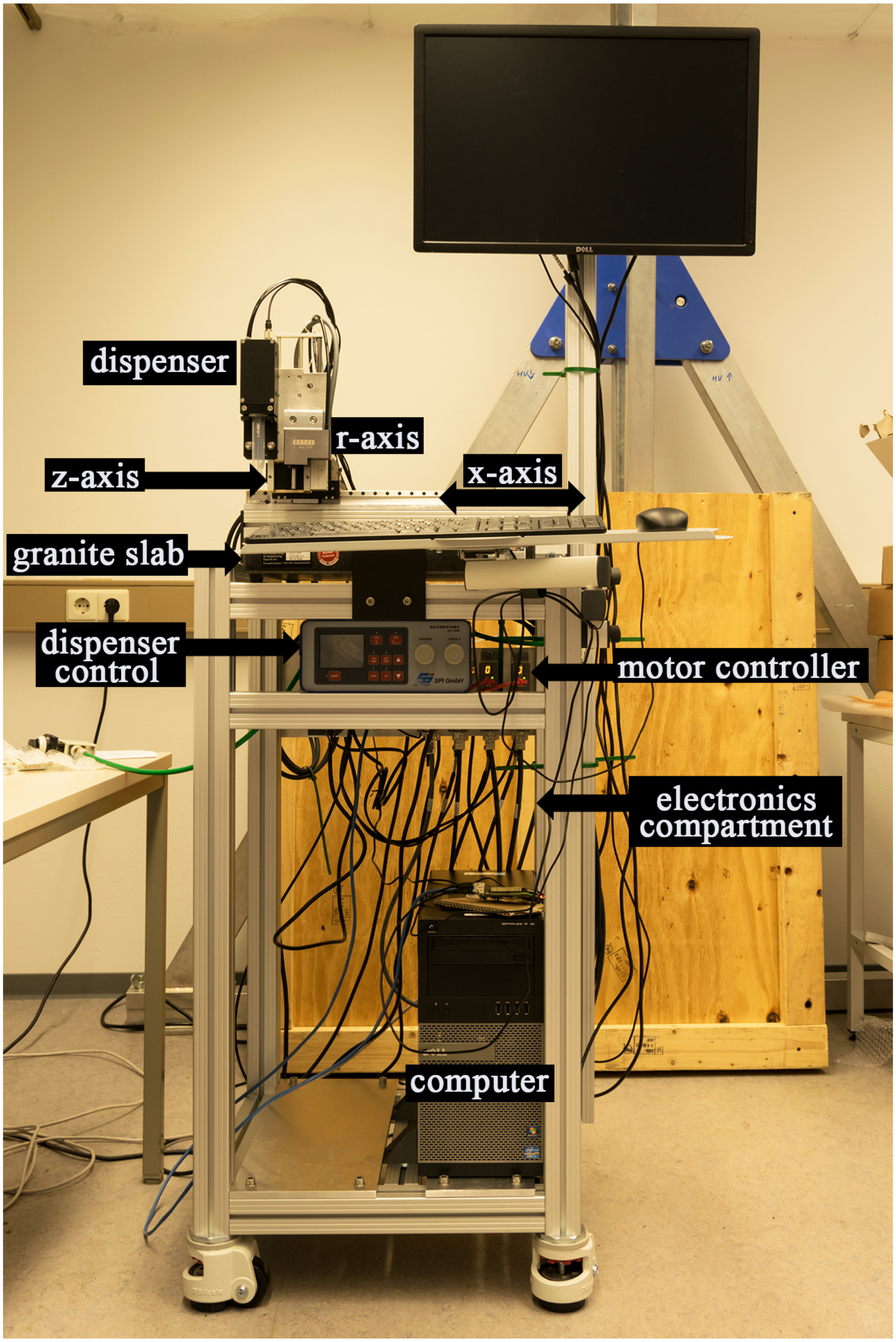

Figure 2.2.: Overview of the glueing robot.

2.2. Axis

Components made by the Swiss company Jenny Science AG are used for all four axes: The x-, y- and z-axis are made of LINAX® linear axes while the r-axis is a ROTAX® rotary motor, see figure 2.1. All four axes are controlled via their own XENAX® servo controller which in turn offers a TCP/IP interface and can therefore be addressed with a regular computer either directly via the interface or via web interface[1] WebMotion® offered by Jenny Science AG. Within this setup all four axes are controlled by a Raspberry Pi using a custom C++ library. Tables 2.1 and 2.2 give an overview of key motor specifications as published by the manufacturer in [6] and [7], respectively.

axis	x	y	z
type	Lxs 400F60	Lxu 320F60	Lxc 85F10
max. travel [Inc]	400 000	320 000	85 000
max. speed [Inc s^{-1}]	4 000 000	3 800 000	2 500 000
max. force [N]	60	60	10
precision [Inc]	± 10	± 12	± 7
repeatability [Inc]	$< \pm 1.5$	$< \pm 1.5$	$< \pm 1.5$
resolution [µm Inc^{-1}]	1	1	1

Table 2.1.: Key parameters of the LINAX® linear motors used for the x-, y- and z-axis [6].

axis	r
type	Rxvp
max. speed [s^{-1}]	1500
max. torque [mN m]	110
max. axial force [N]	180
precision [µm]	$< \pm 10$
repeatability [$''$]	$< \pm 10$
resolution [$''$ $turn^{-1}$]	20.25

Table 2.2.: Key parameters of the ROTAX® rotary motor used for the r-axis [7].

As the x-axis consists of a single motor, mounted on one side of the granite slab (no gantry mode), the y-axis must be strong enough to hold the weight of the z- and r-axis as well as the glue dispenser and structural elements (metal adapter plate) without pitching due to the high torque. A reinforcement has therefore been installed on top of it. Additionally, the z-axis is equipped with a static weight compensator *Geko Lxc 85F10* using compressed air with a maximum load of 3 kg.

[1] The WebMotion® applet requires Java plug-in which is not supported by modern browsers any more. Jenny Science AG therefore offers a modified version of the Quipzilla browser for download on its website (`https://www.jennyscience.ch/en`). A free registration is required.

All linear motors have specific maximal torque and force limits which must not be exceeded. Furthermore, the following equation [4, p. 32] must be satisfied at all times:

$$1 \geq \frac{|F_y|}{F_{y;\,max}} + \frac{|F_z|}{F_{z;\,max}} + \frac{|M_x|}{M_{x;\,max}} + \frac{|M_y|}{M_{y;\,max}} + \frac{|M_z|}{M_{z;\,max}} \tag{2.1}$$

whereby F_i denotes the force acting along and M_i the torque spinning around the i-th axis, see figure 2.3.

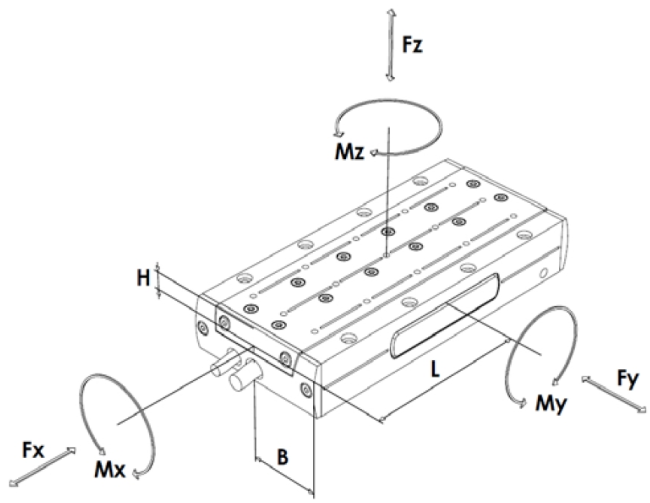

Figure 2.3.: Forces and torques on a LINAX® linear motor [6, p. 24].

Note, that in the following all values were taken from documentation material published by Jenny Science AG which did not specify any uncertainties. Measured and roughly estimated values are provided with an uncertainty big enough to cover any not specifically considered error sources, especially as the whole calculation is considered to be an approximation only. The cumulative weight[2] of the r-axis, the glue dispenser as well as any structural elements mounted on the z-axis is (1439 ± 50) g which is well below the 3 kg limit of the static weight compensator. In the following, a perfect adjustment of the compensator is assumed, however any payload attached to the r-axis (HV-MAPS) as well as a variable amount of glue in the dispenser cartridge are not compensated but light enough to be negligible. Furthermore, small forces arise from pressing the vacuum cup - later mounted on the r-axis - onto the payload. Note however, that HV-MAPS are small in dimension, thin and therefore light as well as very sensitive to pressure, so not too much force must be applied.
All these effects are considered to be marginal because the resulting force is smaller than 1 N which can easily be sustained by the z- and r-axes.

While the z-axis is not loaded significantly and nearly no torque is present (the adapter plate offers a large bearing surface and is fixated by multiple screws, the lever is short), the y-axis is heavily loaded with the z-axis and any mass attached to it. To increase stiffness of the

[2]dispenser: 611 g; adapter plate: 573 g; rotative motor: 180 g; screws, glue, cables: 75 g.

y-axis a rigid boom *Auslegearmierung Lxu 320F60* is attached to its top. The total weight[3] moved by the y-axis motor (the rail is moving, not the sled) calculates to (4869 ± 100) g. The bigger uncertainty of 100 g results from the unknown mass of screws and bolts added during assembly while at the same time an end element of the sled has been removed. In contrast to the vertically mounted z-axis, the y-axis operates horizontally, so the weight itself is not very important. The torque, however, is important, because the more the rail protrudes into the working area, the higher the torque acting on the sled-rail-connection becomes and the higher will the bending of the whole mechanism be. This bending will result in a y dependency of the z position which is not desired and difficult to correct during operation. The spatial mass distribution of the boom is non-trivial because of its shape, however in the following a uniform distribution is assumed, the calculated torque is therefore an upper limit estimation. Additionally, counter-torque resulting from the rail and boom behind the x-axis is not taken into account.
The absolute torque M_i produced by a force F_i acting in a distance r_i from the rotation axis is given by $M_i = F_i r_i$ with the weight force $F_i = m_i g$ of a mass m_i (m_i at distance r_i). The total torque results as a sum over all indices i: $M \coloneqq \sum M_i$
Concerning the given setup the rotating axis of the y-axis (alongside the torque) is parallel to the x-axis, piercing through the middle (centred horizontally and vertically) of the y-axis rail as shown in figure 2.4.

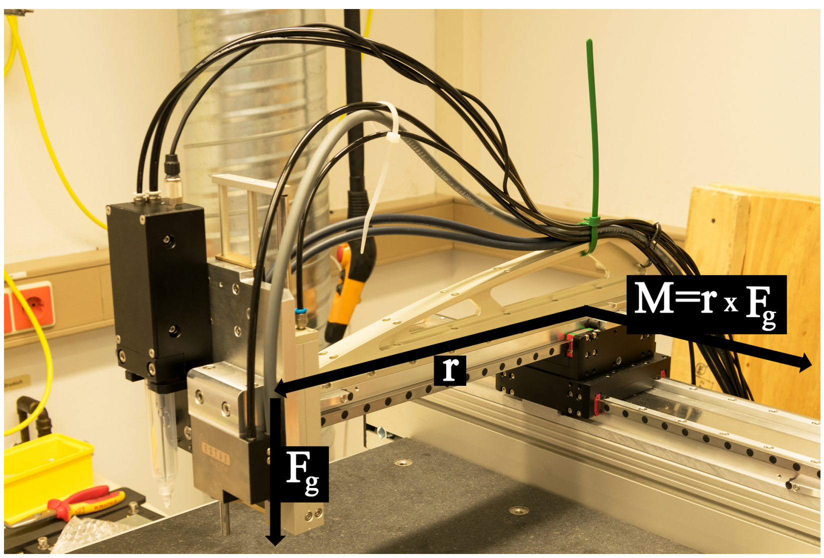

Figure 2.4.: Force F_g and resulting torque $M = M_{\text{boom, rail}} + M_{z\text{-axis}} + M_{\text{load } z\text{-axis}}$ acting on the y-axis sled.

Note that only the section of the y-axis rail on the side of the granite slab contributes to $M_{\text{boom, rail}}$. The distance between the end of the y-axis and the z-axis was measured to be $r_1 = (24 \pm 2)$ mm, respectively $r_2 = (55 \pm 2)$ mm for the load of the z-axis. The measurement was conducted with a caliper and must be seen as a rough estimate because of the complex geometry without the possibility of a fence. Furthermore, the objects are considered to be classical point masses. The maximal torque M_{max} acts, if the y-axis is fully extended (the z-axis moved to the front of the apparatus) to 320 mm (y-position 0 Inc). Another 55 mm must be added due to the sled length, resulting in a lever length of 375 mm. The torque calculates as follows:

$$\left.\begin{aligned} M_{\text{load } z\text{-axis}} &= (1439 \pm 50)\,\mathrm{g} \cdot g(r + (55 \pm 2)\,\mathrm{mm}) \\ M_{z\text{-axis}} &= 830\,\mathrm{g} \cdot g(r + (24 \pm 2)\,\mathrm{mm}) \\ M_{\text{boom, rail}} &= \tfrac{1}{2}\tfrac{(2600 \pm 50)\,\mathrm{g}}{450\,\mathrm{mm}} \cdot gr^2 \end{aligned}\right\} \Rightarrow M_{max} = (13.300 \pm 0.226)\,\mathrm{N\,m}$$

whereby $M_{max} = M(r = 375\,\mathrm{mm})$ and $g = 9.81\,\mathrm{m\,s^{-2}}$. Finally the x-axis has to move all of the components described above as well as the sled of the y-axis which accumulates to be (5819 ± 150) g in total[4]. Again, additional 50 g have been added to the uncertainty to take screws, overlying cables and other material into account.

In the following equation 2.1 shall be verified for all three linear axes (numerical values and notation are taken from [6]):

x $F_x = F_y = M_y = M_z = 0$
$F_z \approx (58 \pm 2)\,\mathrm{N} < F_{z;\,max} = 5400\,\mathrm{N}$
$M_x \leq M_{max} < M_{x;\,max} = 243\,\mathrm{N\,m}$
$\rightarrow$ equation 2.1 fulfilled

y $F_x = F_y = M_x = M_z = 0$
$F_z \approx (49 \pm 1)\,\mathrm{N} < F_{z;\,max} = 5400\,\mathrm{N}$
$M_y \leq M_{max} < M_{y;\,max} = 211\,\mathrm{N\,m}$
$\rightarrow$ equation 2.1 fulfilled

z $F_y = M_x = 0$
None of the two remaining torques and forces vanish due to the complex geometry of the adapter plate, the glue dispenser and the r-axis. However, if the weight compensation is adjusted correctly, F_x is well below its maximal value of $F_{x;\,max} = 10\,\mathrm{N}$. Furthermore, less than $F_{z;\,max} = 1722\,\mathrm{N}$ are needed to hold the payload in place (eight screws). The same eight screws lead to a good force/ torque distribution resulting in M_y and M_z to stay below their maximum of 1722 N m.
$\rightarrow$ equation 2.1 fulfilled

All electronics, mainly consisting of the motor control units, are hidden under the granite slap and mounted directly to the aluminium structure (see figure 2.5). The four XENAX® controllers are mounted vertically besides each other to allow efficient convectional cooling. Communication is realised via a switch which must offer at least five ports (four for the controllers and one for the computer). Additionally, a power supply with a nominal output voltage of 24 V and a maximal current of 20 A supplies power to all components described so far except for the Raspberry Pi which has its own power supply.

[3] load on z-axis: (1439 ± 50) g; z-axis: 830 g; y-axis rail: 1850 g; boom: 750 g.
[4] load on y-axis: (4869 ± 100) g; y-axis sled: 950 g.

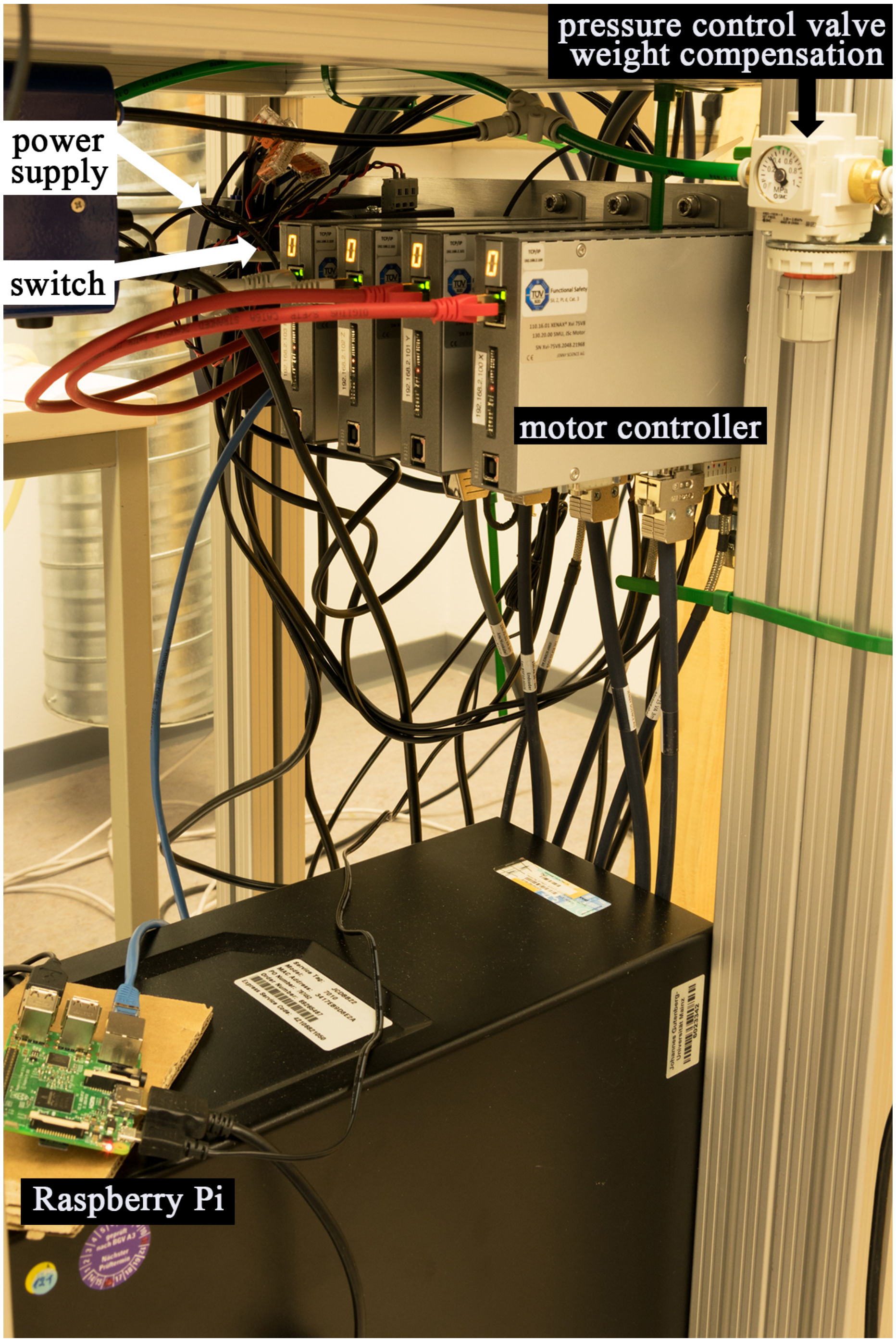

Figure 2.5.: Electronic and computer space below the granite slab. On the top left the trailing edge of the glue dispenser (see section 2.3) is visible. On the top right behind the red cables the four XENAX® are placed on the left of the control valve for the weight compensation. The Raspberry Pi running the C++ software lies on the black computer on the lower left.

2.3. Jet dispenser and pneumatic system

The jet dispenser control device (*Jet DISPENSER JDC-200H*), which applies pressure to the glue dispensing unit on the z-axis, is mounted on the front of the whole apparatus just below the granite slab (see figure 2.7).

The device offers a LCD touch-display on the left which shows all parameters set, different buttons in the mid and rotary controls on the right to set these parameters. The cartridge pressure (*CARTR.-P* or *C-P*) as well as the piston pressure (*PISTON-P* or *P-P*) have to be set manually, by the two rotary controls. While the first one is the pressure applied directly inside the cartridge containing the glue, the second is the pressure applied to the piston to move it up and down. The button section in the middle of the controller can horizontally be divided into two subsections. The upper contains only two buttons for the two operational modes, the *DOT* and the *LINE* mode. By pressing the *SHOT* button, right under the LCD display, the glue is dispensed. In the *DOT* mode, a constant number of shots are dispensed, independent from the pressing duration of SHOT. In *LINE* mode however, shots are released as long as the *SHOT* button is pressed. The lower subsection contains key buttons on the right to lower or raise one of the four settings, whose buttons are next to them:
The *ON TIME* describes the timespan pressurised air is applied to the piston to accelerate it first upwards and then downwards again. The *NUM* parameter sets the number of shots dispensed per pressing *SHOT* and has only an effect in *DOT* mode. Note that in *LINE* mode as well as *DOT* mode with the *NUM* parameter greater than one the *OFF TIME* passes in between two shots. Finally there are 20 channels (i. e. individual sets of parameters) the controller can handle, the channel currently active is selected via the *CH* button.

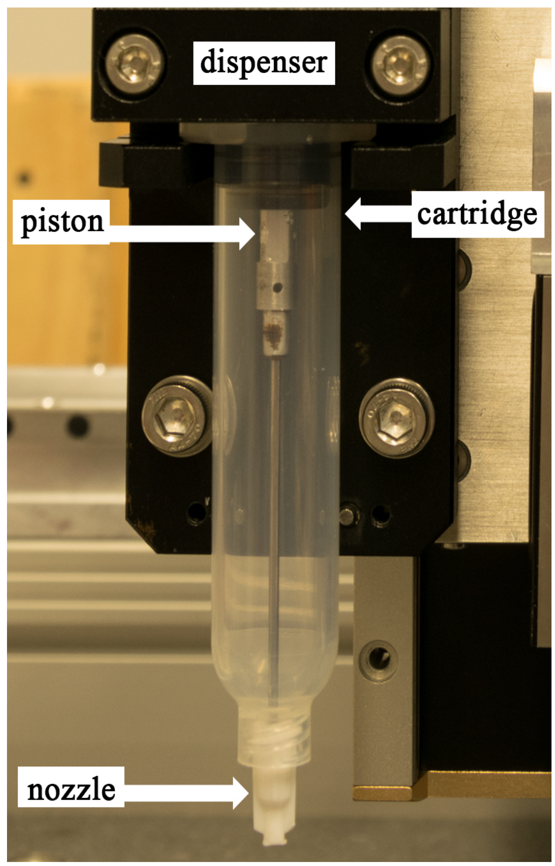

Figure 2.6.: Glue dispensing unit *SG-JE 100* mounted on the z-axis.

The dispensing unit (*SG-JE 100*) shown in figure 2.6 is mounted on the z-axis. Glue is contained by the cartridge and must be accumulated at its bottom in and right above the nozzle. Depending on the viscosity of the glue care must be taken of possible air bubbles when filling the cartridge because they do typically not rise to the surface. The nozzle is the outlet opening for the glue and

mounted at the bottom side of the cartridge with the help of a Luer taper. Finally, there the piston (mounted right in the middle of the cartridge, touching the nozzle on its inside when in lower position) is made to move up and down to dispense one dot whereby it releases the nozzle opening when moving upwards and pushing the glue out when hitting the nozzle on its way down. The momentum transferred leads the glue to be jetted out of the opening onto the underlying surface.
Note that the piston as well as especially the nozzle come in different shapes and sizes. The right configuration is dependent on the explicit application as well as physical properties of the glue (e. g. viscosity).

Figure 2.7.: Glue dispenser control device *Jet DISPENSER JDC-200H* mounted below the granite slab.

The nozzles mainly differ in the diameter of their hole as well as its shape and explicit conical form inside. The pistons come with rounded or sharp edges at their end. The higher viscosity or the more material shall be dispensed with a single shot, the bigger the nozzle must be and the sharper must the piston edges be formed, respectively. Sharper edges mainly lead to a greater momentum transfer from the piston to the glue. Figure 2.8 shows the tip of a ceramic nozzle used for glue dispensing tests (see section 3.3). Note that the opening has a diameter of approximately 150 µm.

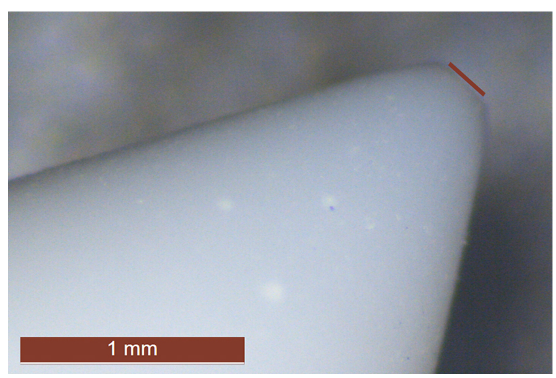

Figure 2.8.: Tip of a ceramic nozzle with an opening diameter of approximately 150 µm

3. Initial operation

In the following the initial setup and basic mandatory settings of all components from section 2 are described. Section 3.1 covers the axes, section 3.2 deals with the calibration of the weight compensator and in section 3.3 the dispensing parameters are investigated.

3.1. Axis

The axes are the most important part of the glueing robot. In the following the interface to control them is explained in greater detail (section 3.1.1) as well as a checklist to establish fundamental parameters for their operation is presented (section 3.1.2).

3.1.1. Interface

Although the C++ interface offers all possibilities to send or retrieve data from the controllers, the WebMotion® applet is easier to use in case of repeated rapid changes in basic parameters (acceleration, speed, smoothing factor, movement to or by a defined position or distance). Furthermore, basic analysis tools (space-time, acceleration-time, deviation-time or force-time curves) are already implemented and do not have to be programmed by the user. Complex programmes may indeed be written within the applet, however the C++ environment offers far more possibilities and especially clarity. Because the latter is not important when setting the apparatus up, in the following the WebMotion® web interface will be used. Note that the Qupzilla browser Jenny Science AG offers does not run on Linux or iOS systems but on Windows only, so instead of the Raspberry Pi a computer running Windows is used.
The IP address of the XENAX® controllers is static within this setup and written on the controllers[1]. If no connection can be established the documentation gives a hands-on approach [4, p. 28]. Once a connection is established the software will run an automatic check for capability of software (firmware) and hardware (motor attached) as well as reading all settings on the controller. Two options can now be chosen from: a quick start, which is a basic function test [4, p. 40], or the full operation mode with the ability to control all parameters. The latter is relevant in the following.

3.1.2. Establish operative condition

The operative condition of any axis requires the careful setting of some parameters which can be (and has been) done by the following steps. These are based on the instructions of the Jenny Science AG manual [5] (see appendix A for screenshots of the tabs used):

1. Make sure the desired axis can be moved in both directions without hazard.
2. Open the *setup - state controller* tab and set *PAYLOAD* (linear motor) or *INERTIA* (rotary motor) according to the weights calculated in section 2.2. Note that the weight

[1] 192.168.2.X with X defining the axis as follows x: X=100, y: X=101, z: X=102, r: X=103.

of the empty sled must not be considered (as done above), it is added automatically by the system (as long as the motor is recognised correctly).

3. Set the gain of the position measurement (*GAIN POS*) by pressing the *Auto Gain* button. The inserted value is theoretical and may be subject to changes later.
4. For rotary motors open the *move axis - by click* tab and let the system supply voltage to the motor by clicking *Power Cont*. Thereafter check whether torque can be applied to the motor axis.
5. Open the *move axis - by click* tab and initialise the referencing process by clicking *Reference*. The LINAX® motor will move a small distance and reference its absolute position. The ROTAX® motor will do the same by rotating by a small angle. Listen for vibrations.
   If vibrations occur and step 5 is executed for the first time:
   a) Make sure the payload/ inertia parameter set in step 2 is correct.
   b) Repeat step 5.

   If vibrations occur and step 5 has already been executed before:
   a) Open the *setup - state controller* tab and vary the *GAIN POS* setting.
   b) Repeat step 5.
6. Disconnect supply voltage to the motors by clicking *Power Quit* and set the *SOFT LIMIT POS* values *SLP-* and *SLP+*.
7. Lock any motor not considered during this process in position. This can easily be done by pressing *Power Cont* on the *move axis - by click* tab.
8. Set speed *Speed*, acceleration *ACC*, speed overwrite *SP OVERRIDE* to the maximal value, the smoothing factor *S-CURVE* to the minimal value and *Wait Reverse* to $t = 200\,\text{ms}$. Move the sled with *Go Position* to position $p_1 = SLP- + 2000$ and insert $(SLP+) - p_1 - 2000$ into *Rep Reverse* so that the motor will start moving from the start position (p_1) to the end position $p_2 = (SLP+) - 2000$, rest for a time span with length t and return to its start position p_1. The process repeats after t until the movement is stopped at any point by pressing *Stop Motion*.
9. Open the *move axis - motion diagram* tab, select *DEVIATION* in the drop-down menu and record a new measurement (deviation between actual and target position as a function of time) over a time span of own discretion. Vary the payload defined in step 2 until the deviation before the motor reaches its target position is minimised. Note that a negative deviation mainly results from a payload being too small and vice versa. Listen for vibrations (these may occur specifically on a small segment of the whole drive).
10. Open the *setup - state controller* tab and vary *GAIN POS* until vibrations encountered during step 9 are minimised. If no vibrations occur, minimise the general volume the motor produced whilst moving. Move on if vibrations cannot be eliminated in its entirety.
11. If vibrations could not be eliminated in step 10, open the *Advanced* slide of the *setup - state controller* and decrease the *STAB-DYN* parameter.
    If no sufficient progress can be made, analyse the spectrum by clicking on the <*Scan*> button and follow the steps in the XENAX® manual [4, p. 75].

12. Open the *move axis - motion diagram* tab, set speed *SPEED* to its maximal and acceleration *ACC* to its minimal value. Slowly increase the latter until *error 50* (deviation between calculated target and currently measured position is greater than the allowed value set in *Deviation POS ACT* in the *setup - state controller* tab) will be thrown or the value of the Cycle Calculator is reached. Note that the Cycle Calculator is only available to Jenny Science AG.
    The maximal dynamic is then given by $0.9 \inf a_{50}$, with a_{50} being the acceleration at which *error 50* occurred.

After every axis has been set up according to the above steps, let all axes move together and eliminate possible vibrations:

1. Open the *move axis - motion diagram* tab and set the speed overwrite parameter *SP OVERRIDE* to 5 % for every axis. The axes will move with no more than $0.05 v_{target}$, with v_{target} being the target speed set.
2. Let all axes move together in between p_1 and p_2 with 200 ms *Wait Reverse* time and listen carefully for any vibrations.
   If vibrations occur, vary parameters as follows until vibrations are minimised:
   a) Use a negative value for *STAB-DYN* on the *setup - state controller* tab.
   b) Avoid frequency with *Avoid vibration FREQ* on the *setup - state controller* tab.
   c) Set a lower value to *GAIN POS* on *setup - state controller* tab.
   d) Open the *move axis - by Forceteq®* tab and start the *FORCE CALIBRATION* for every axis by entering the soft limits into *START* (*SLP-*) and *STOP* (*SLP+*), activating the checkbox *SERVO ON* and finally pressing the *Start* button.
      The calibrations measures magnetic friction forces caused by design of the axes which are then automatically counteracted. [4, p. 58] Data acquired is saved on the XENAX® controllers and stays valid as long as the setup is not changed.

All parameters used for the setup are listed in appendix B for each axis. Varying the main motion parameters (acceleration, speed and smoothing factor) leads to the following insights:

The smoothing factor s is positively correlated with jerk. A smoothing factor of 0 % corresponds to an ideal and abrupt movement with instant and therefore infinite acceleration. (Note that the smallest value is $s = 1\,\%$.) Speed and acceleration are set as target (and therefore maximal) values, they may not be reached depending on distance, acceleration and speed (e. g. the sled will not reach a high speed on a sufficient short distance if the smoothing factor is high and hence acceleration is increased slowly) as shown in figure 3.1a.

Figure 3.1b shows the deviation from the target position of the x-axis while travelling over the full available distance of 400 mm from position 0 Inc to 400×10^3 Inc. The blue curve was measured with the maximal smoothing factor and a rather low acceleration and speed. The deviation varies rapidly in a range of -15 Inc to 15 Inc over the whole distance, bigger swings are rare. In contrast to the blue curve the green and red were measured with higher acceleration and speed, but differ in the smoothing factor. While the red curve ($s = 100\,\%$) exhibits larger oscillation at the beginning and end of the motion it is in general comparable to the blue one. The green curve ($s = 50\,\%$) however shows extreme amplitudes, especially at the end when the moving sled is decelerated quickly (compare with the speed in figure 3.1a). With high acceleration, deviations accumulate to much bigger values in a given time than at lower speeds.

Because the final deviation from the end target position of the movement does not depend on the deviation during the movement, the above results are not directly relevant for the assembly of the detector modules. However, because continuous readjustments by the controller increase vibrations of the whole apparatus, which affect the accurate placement of the HV-MAPS, it is advantageous to minimise them. Because the assembly of the HV-MAPS does not require high target speeds or accelerations they should be reduced to a sufficient low value. Then the smoothing factor is less relevant for a vibration free movement and can therefore be chosen much smaller than 100 %. This also minimises material stress (bigger corrections at low frequency in favour of small ones at a high frequency).

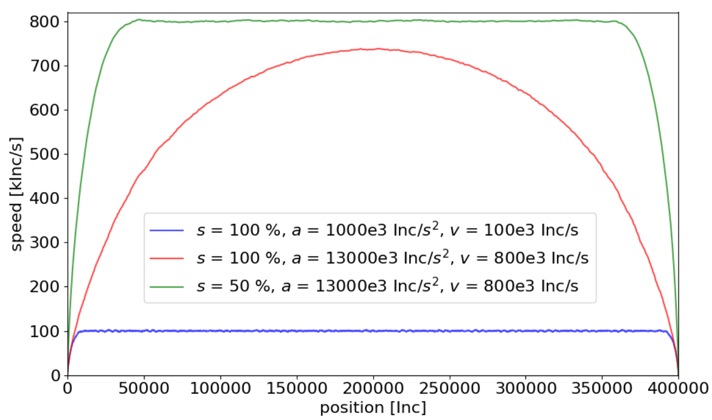

(a) Speed of the x-axis.

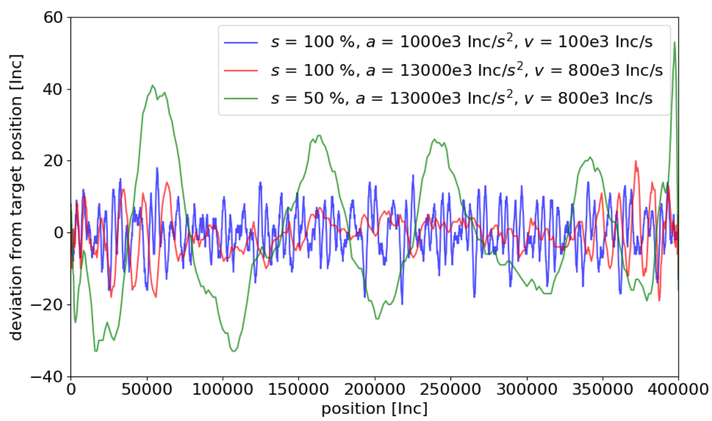

(b) Deviation from target position.

Figure 3.1.: Deviation and speed of the x-axis as a function of position with different target speed v, acceleration a and smoothing factor s. The x-axis was moved over the full available distance of 400 mm from 0 Inc to 400×10^3 Inc.

3.2. Weight compensation

The weight compensation on the z-axis allows to attach payloads with greater weigh force than the maximal force the axis can handle. Pressurised air is then used to statically compensate the weight force so the axis can still be operated as it just has to move the inertial mass (force exerted by the motor equal for up and down movements).

3.2.1. General description

The weight compensation of the z-axis works with compressed air which is confined in a cylinder right beneath the r-axis as shown in figure 2.1. A piston is attached to the motor sled and moves inside this cylinder, the compressed air forces the piston up while at the same time it is being pushed downwards by gravity (weight force of any mass attached to the z-axis as well as the z-axis sled).
Concerning the specific setup of the glueing robot, pressurised air fed into the pneumatic system of the robot via a simple on-off valve which enables the robot to be moved without the need of depressurization. From this valve a single tube goes off which is later divided to feed the jet dispenser as well as a pressure control valve. The latter enables the pressure of the weight compensation to be adjusted within 0.05 bar.
The total volume of the compensation system is finite but dependent on the position of the z-axis. If the (hollow) piston is completely withdrawn from the cylinder (z-axis in position 0 Inc), the volume is maximal and vice versa so with a total travel of approximately 79 000 Inc and a piston radius of (4.00 ± 0.05) mm the total volume changes by $(3.97 \pm 0.10)\,\mathrm{cm}^3$. Despite the volume change pressure inside the system remains the same, regardless of the z-axis position. The above mentioned control valve dissipates air into the laboratory if pressure rises and opens towards the supply if pressure drops. Therefore pressure inside the compensator can never be higher than supplied to the control valve. Note this is only true if the supply pressure is not lowered after the initial filling. If this happens, the compensator enters an undefined state depending on the movement of the z-axis, its position at the time of lowering supply pressure and the amount of leakage. To avoid this undefined state the control valve should be opened towards the laboratory (i. e. a very low nominal pressure shall be adjusted) and closed again (i. e. the desired pressure shall be adjusted). If, in turn, supply pressure is raised, no actions need to be taken.

3.2.2. Pressure adjustment

Ideally the pressure inside the compensation system leads to a force $F_p = -F_g$ exactly counteracting the weight force of any attachments to the z-axis, so the axis is in equilibrium. The motor would then be able to move the z-axis sled with minimal effort, minimising force (and therefore current applied to the coils inside the axis) and leading to a smoother and more accurate drive. Accuracy, especially deviation from target position during movement, should increase with less force needed because the amplitude of corrections made by the motor control is smaller. The nominal pressure P_{nom} needed to achieve a total compensation is given by

$$P_{nom} = \frac{F_g}{A} = \frac{(m_{\text{load } z\text{-axis}} + m_{\text{sled } z\text{-axis}})g}{\pi r^2} \approx \frac{((1439 \pm 50)\,\mathrm{g} + 230\,\mathrm{g})g}{\pi(3.90 \pm 0.05)\,\mathrm{mm}} = (3.49 \pm 0.11)\,\mathrm{bar}$$

with F_g being the weight force to be compensated and A the area (circle with radius r) the force F_g acts on, whereas g is the gravitational acceleration constant.
Note that the above calculation does not take any cables and tubes into consideration. The r-axis is equipped with a single, sturdy and a rather thick power supply cable with a diameter of approximately 8 mm. Furthermore, a thin tube with a diameter of about 4 mm is attached to its rear side and may be used to supply pressurised air or vacuum directly to the hollow shaft. Cable and tube contribute only moderately to the total weight but their sturdiness leads to significant force exertion. When the z-axis moves, it stretches and bends both strands so the final force with which they act on the z-axis is neither constant nor in any way trivial to calculate.

In order to determine the pressure P_{ex} for perfect compensation experimentally, a measure of the applied force must be found. The current I supplied to the motor by the motor control is directly proportional to the force F applied and given by

$$I = cF \qquad \Leftrightarrow \qquad F = \frac{I}{c}$$

with the proportionality constant $c = 0.28\,\mathrm{A\,N^{-1}}$ [4, p. 97] (saved on and automatically used by the motor controller) specifically for the z-axis. Note that the forces are measured with a resolution of $0.25\,\mathrm{N} \mathrel{\widehat{=}} 0.07\,\mathrm{A}$ and a minimal measurable force of $F_{min} = 0.5\,\mathrm{N} \mathrel{\widehat{=}} 0.14\,\mathrm{A}$. [4, p. 97] As stated in table 2.1, a maximal force of $F_{max} = 10\,\mathrm{N} \mathrel{\widehat{=}} 2.8\,\mathrm{A}$ can be achieved.
Because the motor control offers an easy current read out possibility, it was decided to move the z-axis while reading out the current I as a function of time. The current $I(t)$ is then converted into a force $F(t)$ which is numerically integrated over a specific domain. Integrals for different pressures applied to the weight compensation are compared in the aftermath. If the pressure is adjusted correctly, the motor should only need force to accelerate and decelerate the inertial mass as well as to compensate friction.
Since opposite directions of travel are accomplished by opposite polarity of the supply voltage, the current $I(t)$ (and $F(t)$) is a signed quantity. Thus moving the motor periodically up and down in between two positions z_1 and z_2 with the same acceleration and absolute target speed should lead to a vanishing integral over whole periods. Note that any friction leads to a signed offset and should therefore not influence the measurement because it also cancels out.
Because high acceleration a leads to significant peaks of $F(t)$ especially at the beginning and end of an acceleration phase (while approaching/ departing the turning points z_1 and z_2), acceleration should be kept as small as possible. Additionally, the smoothing factor s should be maximised to increase a slow and smooth travel of the motor. Target speed v must be sufficiently high to be able to take enough data in a reasonable amount of time but also small enough to be reached and stably maintained, avoiding larger overshoots. A reasonable amount of waiting time in rest at the upper and lower position should be included to prevent any vibrations from accumulating and affecting the measurement.

Since WebMotion® offers an easy possibility to retrieve and save the desired data (tab *move axis - motion diagram*) for a maximal time period of 8 s, the following parameters were chosen:

$$z_1 = 30 \times 10^3\,\mathrm{Inc} \quad z_2 = 59.2 \times 10^3\,\mathrm{Inc}$$

$$s = 100\,\% \quad a = 2500 \times 10^3\,\mathrm{Inc\,s^{-2}} \quad v = 11 \times 10^3\,\mathrm{Inc\,s^{-1}}$$

Note that $z_0 := \frac{z_2+z_1}{2} = 44\,600\,\mathrm{Inc}$ is roughly the mid of the maximal travel (approximately 80 000 Inc) where the sled is entirely covered within the motor rail. The situation is therefore completely symmetric with a distance of $\Delta z = 14\,600\,\mathrm{Inc}$ to be driven up and down.

To be able to start and stop the measurement according to the movement the following programme in the *application - program* tab was set up:

```
1) EXECUTE INDEX 1
2) WAIT TIME 1000 ms
3) EXECUTE INDEX 2
4) WAIT TIME 1000 ms
5) EXECUTE INDEX 3
6) PROGRAM END
```

All three indices were defined in the *application - index* tab as shown in table 3.1.

index	*ACC x1000* [kInc s^{-2}]	*SPEED* [Inc s^{-1}]	*DISTANCE* [Inc]	*type*
1	2500	11 000	30 000	*ABS*
2	2500	11 000	59 200	*ABS*
3	2500	11 000	44 600	*ABS*

Table 3.1.: Indices defined to be used with the weight compensation test programme.

According to the above mentioned programme and indices, the motor first moves towards position z_1, holds for 1 s before continuing down to z_2, resting again for 1 s and finally moving towards its end position z_0. Note that the operator has to move the axis to the initially desired position z_0 by hand (e. g. via the *move axis - by click* tab). Finally, data can be taken by selecting *LOGGING AUTO*, clicking the *record new* button and commanding *PGx* in the *move axis - motion diagram* tab. Thereby x needs to be substituted by the correct number the above programme is saved at.

The algorithm described above has been executed 10 times for pressures from 3.4 bar to 3.8 bar in intervals of 0.1 bar. Note that all data sets retrieved exhibit exactly 3805 data points which corresponds to a total measurement time of 7.61 s because values are read every 2 ms. For every measurement $1 \leq i \leq 10$ and pressure P the force $F_{Pi}(t)$ has been integrated numerically and averaged over all 10 measurements. Because a linear dependence between integral and pressure is suspected a linear function $(mx + b)$ is fitted to the data. Its root then corresponds to P_{ex}.
For each pressure P figure 3.2 shows an exemplary force measurement ($F_{Pi}(t)$ as a function of the arbitrary data array index). The increasing force needed for smaller pressure can clearly be seen, note especially the green ($P = 3.6\,\mathrm{bar}$) graph being closest to the $F = 0$.

Figure 3.3a shows the mean integral J as a function of pressure P. Data is shown in blue, the linear fit in orange and its root $P_0 = (3.57 \pm 0.80)$ bar in red, corresponding residuals are presented in figure 3.3b.

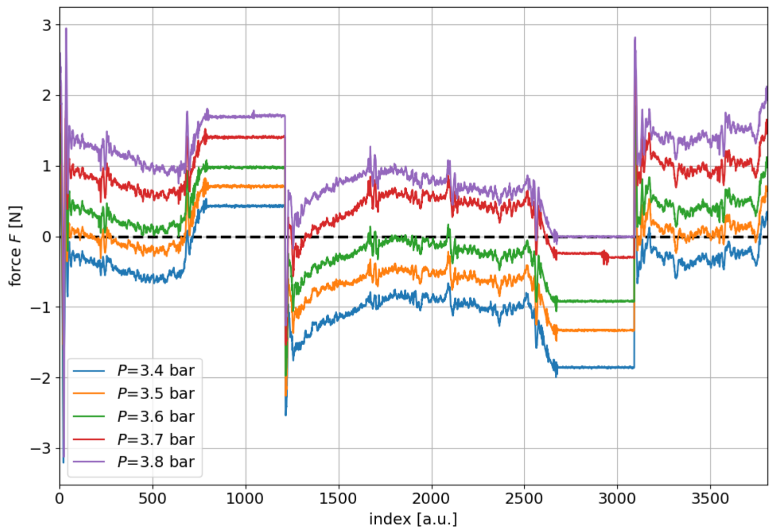

Figure 3.2.: Exemplary force profiles F_{Pi} for every pressure P applied.

Note that the linear fit passes well within the error intervals of the pressure P but outside of those of the integral J. The reduced chi-squared $\chi_{red} = 0.04$ indicates overestimated errors while p- and r-values match perfectly to the suspected linear coherence which is also clearly visible in figure 3.3a. The uncertainties of the fitting parameters are also large with about 16 % both for the slope m and y-intercept b.
Note the major error bars on the pressure P, which result from the rather rough division ($0.2\,\mathrm{bar}\,\mathrm{DIV}^{-1}$) of the pressure control valve scale. However, the fit passes the data points only in near distance (see also figure 3.3b) which, in combination with the small χ_{red}, implies that the uncertainties have been overestimated. Figure 3.3b shows the residuals whereby the J-error must be understood as the pressure error converted with the help of the slope of the fitted linear function.
It must be noted that all the above uncertainties are a result of the tremendous initial error of the pressure P which can only be reduced with a better and more accurate pressure measuring method/ equipment.

The experimental result P_{ex} differs from the nominal pressure P_{nom} by $\Delta P \coloneqq P_{ex} - P_{nom} = (0.08 \pm 0.81)$ bar, so in reality more pressure and therefore a higher counteracting force F_p than calculated is needed, even though the difference is minimal. This is consistent with the assumptions made above which neglected the influence of the r-axis cable and tube. Furthermore, the metal bar, the two braces and the piston itself, all of which connect the weight compensator with the z-axis sled, were not included into the weight calculation. The difference ΔP seems plausible in value.

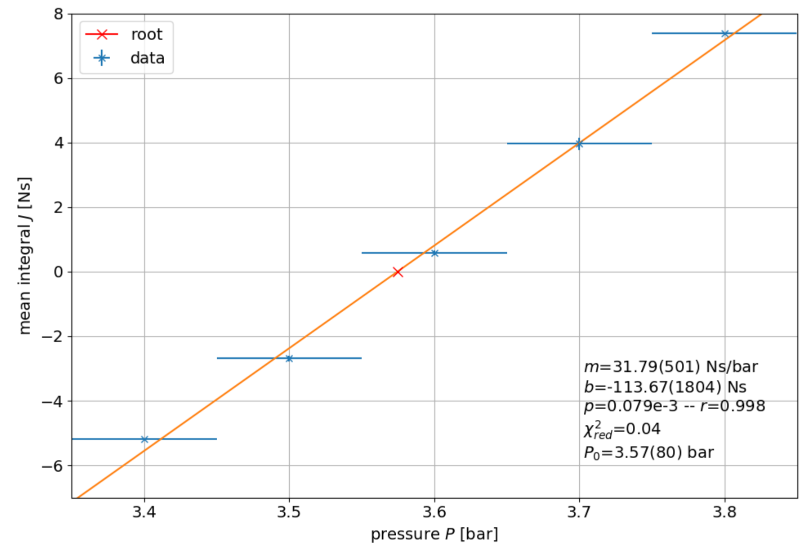

(a) Mean numerical integral J, data is blue, linear fit in orange with root $P_0 = (3.57 \pm 0.80)$ bar in red.

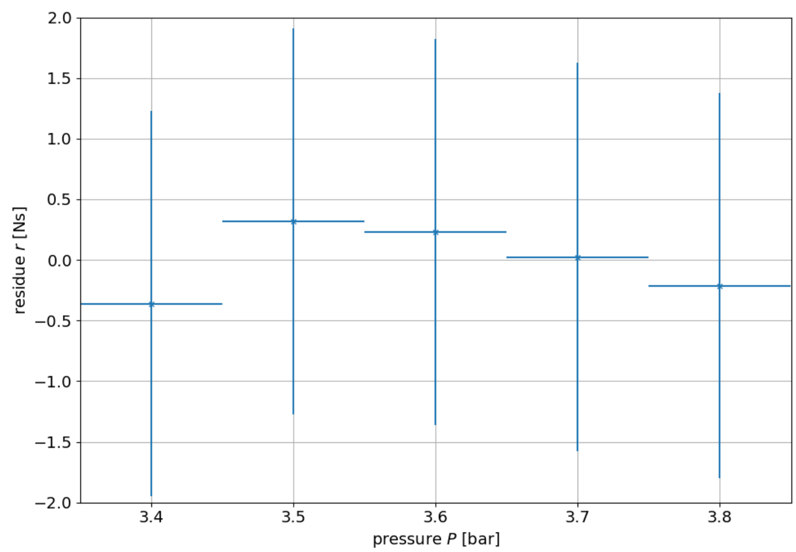

(b) Residuals of the mean numerical integral J.

Figure 3.3.: Mean numerical integral J of the force exerted by the z-axis during one period of movement as a function of pressure applied to the weight compensation system.

For the further operation of the robot a pressure of $P_0 := P_{ex} \approx 3.6$ bar seems to be suitable. Note that the scale of the pressure control valve cannot be read to greatest detail and further weight (a suction cup on the r-axis shaft, glue in the dispenser) may be added in future, so the counteracting force F_p needs to be slightly increased compared to the above result.

3.3. Jet dispenser

The glue used to hold the HV-MAPS into place is dispensed with a jet dispenser as described in section 3.3. In the following a general description of the adjustable parameters is given (section 3.3.1) before developing and executing a method for quantitative analysis of the dispensed glue dots (section 3.3.2).

3.3.1. General description

All in all there are five parameters which can be varied: The piston and cartridge pressure, the on- and off time as well as the distance in between nozzle and underlying surface the glue is dispensed onto. The parameters have the following effect:

cartridge-pressure If the cartridge-pressure is too low, the glue is not pressed into the fine end of the nozzle after the piston has moved upwards, so when it comes down again there is no material to be dispensed and only air will exit the nozzle. With increasing pressure at least some glue may enter the nozzle but still not enough to be fully detached as a drop. Typically this material distorts any following shots (i. e. by deflecting them by angles up to approximately 50° to a vertical plumb line). If the cartridge-pressure is too high, glue exits the nozzle without any piston movement.
In general the higher the viscosity of the glue, the higher the cartridge pressure needs to be set.

piston-pressure The higher the piston-pressure, the more the piston is accelerated and the larger its momentum when hitting the nozzle. If the momentum transferred to the glue is too small, no glue will be dispensed, if it is too high the shot may not be precise enough in terms of position and dispensed mass. Note that the whole apparatus vibrates with every shot. In fact, a too high momentum may lead the dispensed glue to splatter on the surface, causing numerous satellites of unpredictable size and shape around the main dot.

on-time The longer the on-time, the longer will pressurised air move the piston upwards as well as downwards again, thus increasing its maximal distance to the nozzle, its momentum and the time glue can flow into the nozzle. The shorter the on-time, the sharper and quicker is the shot.

off-time The off-time describes the time to pass in between two shots. This has only an effect if more than one shot is dispensed when pressing the *SHOT* button (if *NUM* is greater than 1 or in *LINE* mode).
If the off-time is too short, glue will not be able to flow into the fine end of the nozzle sufficiently which will have the same effect as a too low cartridge-pressure.

distance The larger the distance in between nozzle and underlying surface, the more is the jet influenced by the surrounding air. This mainly concerns its speed and therefore momentum which may influence the shape of the glue dot on the surface as well as the number and location of any satellites. Furthermore, larger distances lead to bigger deviations of the final glue dot from its target position right under the nozzle. In general the result will be more precise for smaller distances.

Note that the five parameters described above are not independent, so varying one of them may lead to a necessity of changing others to get a sufficient/ adequate/ acceptable result. Furthermore, the glue itself may influence the result because of viscosity as well as surface tension. The drop dispensed may not fully fall down but bisect somewhere, whereby the lower part falls down and the upper is withdrawn into the nozzle.

3.3.2. Parameter adjustment

Since the first three parameters described in section 3.3.1 are not independent (the off-time is irrelevant for single dots as used in the following), it is difficult to set them up properly. To find the right settings and optimise them systematically, an iterative approach is needed. So by trial and error an initial parameter set is determined and systematically varied in every component while all the others remain constant on their initial value. After a qualitative and quantitative analysis of the results the initial set is changed to values suiting better before repeating the variation in every component. The process will converge towards an optimal set of parameters.
Note that the initial parameter set is determined by pure trial and error.

When glueing HV-MAPS onto a flat surface, the glue layer is expected to be homogeneous in thickness and purity (no air bubbles enclosed) as well as symmetric. This can be achieved most easily by circular glue dots of constant mass and radius. During the process of finding the initial parameter set it was discovered that the basic shape of glue dots can be described by an ellipse or a thick line, so two attributes characterise a dot qualitatively well.
In order to achieve symmetry and repeatability of the exactly same shape, satellites must be avoided at all costs. Again, it was discovered that they typically occur in two classes of severity, firstly they are still attached to the main dot so that they are somewhat protracted and secondly they are fully separated from the main dot by several millimeters (note the typical diameter of the dots to be about 1.5 mm).
Finally, the ratio of the half-axes and area of the dots (in case they are ellipses) can be determined by overlaying a magnified image of the dots with two circles, one incircle with radius r_1 (semi-minor axis) and one circumcircle with radius r_2 (semi-major axis). The images were taken at a magnification of 6 with an optical microscope attached to a computer, where images taken could be analysed right away with the corresponding microscope software. In case the dot is nearly a perfect circle, only one circle is used ($r_1 = r_2 = r$) so the area A is given by $A = \pi r^2$ with a half-axes ratio e of $e = 1$ per definition. In case a clear ellipse the area evaluates to be $A = \pi r_1 r_2$ with $e = \frac{a}{b}$, whereby a is the half-axis in an arbitrary but constant x-direction and b the half-axis for the y-direction, respectively. Figure 3.4 shows exemplary the evaluation standards for a circle as well as satellites of category 1 (satellite still attached to the main dot). All example images used as evaluation standards are presented in appendix C.
Note that for the numerical analysis of the area and half-axes ratio no systematic errors (placement of the circles over the glue dots by hand as well as optical distortion and digitisation errors of the microscope) were taken into account as they are very small compared to the statistical fluctuations.

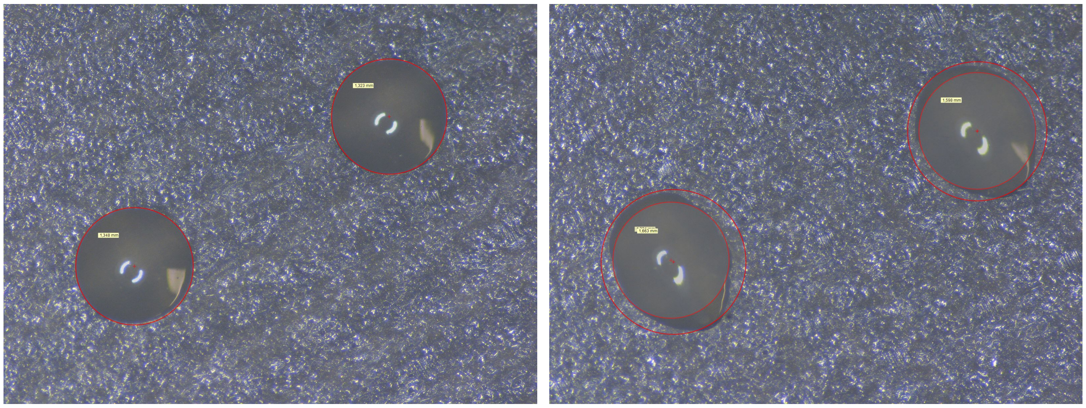

(a) Circles (both dots). (b) Ellipses (both dots).

Figure 3.4.: Exemplary evaluation standards (circle and ellipse) for glue dots.

Additionally, the mass of the dots is of interest. Firstly, the material budget has to be kept minimal in the detector, so if more than one parameter set is possible according to the above mentioned properties, the set with the smaller dot mass is preferred. Secondly, the material should be distributed uniformly so particles get affected independently of their track. Thirdly, all HV-MAPS should have the same adhesion. Because of the extremely small mass of a single dot, several tenth of dots have to be weighted together to generate measurable masses (balance capable of measuring 0.1 mg). This allows only the determination of the mean dot mass but no measure of dispersion. Due to time and equipment limitations it was not possible to use the confocal microscope to generate a 3d-model of individual dot and calculate their mass according to their density. Further research has to be done on this.

All in all, the dots should be circular, of equal mass and area and have no satellites.

The general method has been tested with the single component epoxy resin *Strucalit® 3060 N* which is hardened by heat only. The glue has neither been tested for radiation hardness nor its outgassing properties and can therefore not be used in the final setup. Furthermore, the HV-MAPS shall not be exposed to greater temperatures of 80 °C in contrast to the 120 °C needed by the glue to harden. The main advantage of a single component glue is the long (several hours) handling duration without a significant change in physical and chemical properties. Experience gained with these tests was used to redo the calibration with the single component epoxy resin *DYMAX® Multi-Cure® 6-621* which was found to be suitable for detectors [11] as well as being hardened by heat or UV-light.

In the following only results gained with *DYMAX® Multi-Cure® 6-621* are being discussed: After a non-systematic trial and error phase the initial parameters were set to

$$P_{\text{piston}} = 70\,\text{kPa} \quad P_{\text{cartridge}} = 25\,\text{kPa} \quad T_{\text{on}} = 150 \times 10^{-4}\,\text{s} \quad d_{z\text{-axis position}} = 75 \times 10^{3}\,\text{Inc}$$

Finally, each parameter was varied (except for the z-position d) around its initial value, leaving the remaining constant. Upper and lower bound of the variation process were determined by eye: As soon as the result became consistently affected by satellites, line shape or glue did not exit the nozzle properly any more, the bound was reached. For each parameter set 20 dots were evaluated. The mean dot mass was acquired by weighting a total of 20 samples with 30 dots each, however due to time limitations only about half of the parameter sets were probed.
Note in general, that with decreasing viscosity it is easier to find an initial parameter set because even large variations do seemingly not change the glue dots if evaluated by eye only. With the viscous *Strucalit® 3060 N* (viscosity of 42 Pa s to 46.5 Pa s [12]) the initial set was tedious to find but unambiguous. With the more inviscid *DYMAX® Multi-Cure® 6-621* (viscosity of 0.8 Pa s [10]) the piston-pressure and on-time can be varied in a wide range without noticeable effect on the dots.

Figure 3.5 shows exemplary the measuring results for area A, half-axes ratio e, mean mass m as well as satellite and line number under variation of the piston-pressure P_{piston}. All other diagrams resulting from variation of the on-time as well as cartridge-pressure are shown in appendix D.

Note that during the whole process only statistical fluctuations were taken into account because they are much larger than the precision achieved by the operator when deciding position and radius of the circles placed on top of an image. Any errors resulting from taking a digital image or lens distortions of the optical apparatus of the microscope are considered to be several orders of magnitude smaller than the radii measured and therefore negligible.

The most important quantities are the line and satellite numbers as well as the half-axes ratio because they determine the general geometric of the glue dots. Most notably is the always vanishing line number (red crosses) for all three varied parameters. Severe satellites of category 2 (orange points) have only occurred for (especially) large and small (near boundary) piston-pressures as well as once for 75 kPa, right above the initial value of 70 kPa. All other parameters did not show such a behavior.
It seems plausible that due to the low viscosity of the glue the dispensing process is, at a higher level, invariant for defining a preferential direction in which the glue is shot. Furthermore, inviscid fluids do require less force to reform a more round drop in the air or on the surface they are dispensed onto to minimise surface area, assuming surface tension and adhesion forces to be constant. Because the latter are unknown or difficult to estimate no further investigation has been done. With less force needed a less advantageous shaped dot may change in a more circular one more often.

In contrast to these desired properties of low line and satellite 2 numbers, satellites of category 1 (blue points) occurred often for all three parameters varied. Depending on the parameter up to 8 of 20 dots showed a satellite with a tendency to higher occurrence rates (in case no satellites of category 1 were observed no blue point is visible in the diagrams to allow the more severe category 2 to be displayed). If the majority of these satellites is oriented the same way a preferential direction may be present because the drops are not

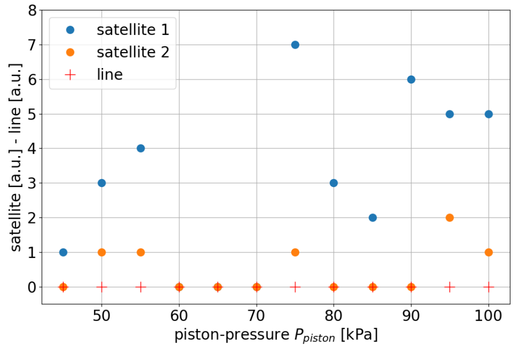

(a) Satellite and line number.

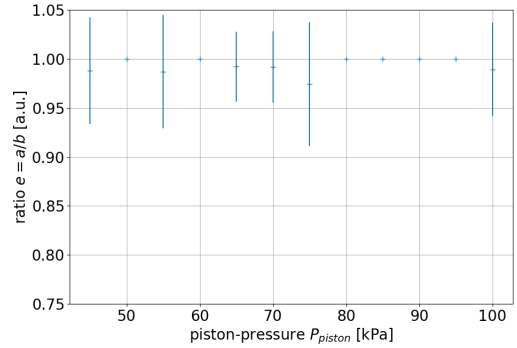

(b) Half-axes ratio $e := \frac{a}{b}$.

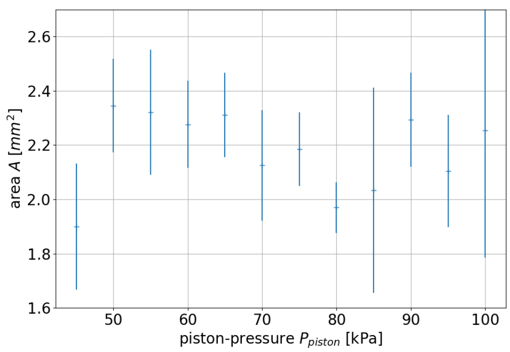

(c) Area A.

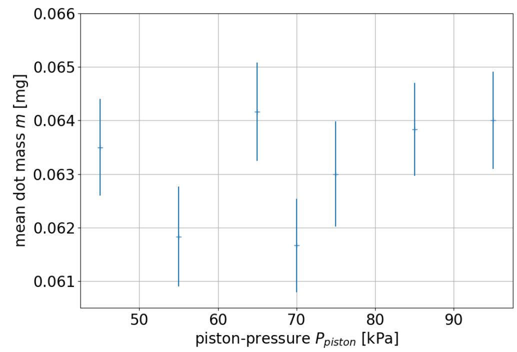

(d) Mean dot mass m.

Figure 3.5.: Exemplary statistics on area A, half-axes ratio e, satellite and line number as well as mean mass m of the glue dots under variation of the piston-pressure.

dispensed vertically downwards but at an angle. But this should also affect he the half-axes ratio by leading to ellipses instead of circles.
Taking the half-axes ratio into account a preferential direction cannot be verified. For ratios unequal to the optimal value of 1 (only circles, no ellipses) relatively large statistical fluctuations for low satellite numbers in between 60 kPa and 70 kPa occurred, but for ratios equal to 1 medium satellite numbers in between 80 kPa and 95 kPa are present. At the same time relatively small satellite numbers correspond to mostly non optimal ratios in between 45 kPa and 55 kPa. On-time and cartridge-pressure do also not indicate a correspondence between satellite number and half-axes ratio.
It must be noted that any deviations of e from its optimal value of 1 are smaller than 0.025 a. u. and any statistical fluctuations remain (if non vanishing) around ± 0.05 a. u. (except for maximal cartridge-pressure of 40 kPa).
The single outlier at a cartridge-pressure of 40 kPa cannot be explained properly. The existence of a preferential direction (high pressure leads to glue spillage without piston movement - small amount of glue attached to the nozzle influences the dispensed glue) seems unlikely because of the vanishing satellite numbers and could not be observed during the experiment.

The area a glue dot covers is independent on its mass as a higher momentum transfer and a smaller viscosity lead to bigger area covered upon hitting the surface. Furthermore, a low viscosity leads to dissolving dots.
Piston-pressure as well as on-time are the parameters to define the momentum transferred, so a correlation in between them and the area is expected. While the on-time does indeed show such a behaviour the piston-pressure clearly does not do so. But even more surprisingly the cartridge-pressure, which would have absolutely no influence on the area, does (see figures D.1c, D.2c and 3.5c).
The correlation shown by the on-time is clearly positive and seems to be linear within error intervals (a quantitative analysis has not been conducted due to the poor data basis). The mean dot mass shows no dependency on any other quantity or parameter and stays, except for one outlier at 225×10^{-4} s, rather constant. A slight inclination towards longer on-time can be suspected nonetheless.
Concerning the piston-pressure the statistical fluctuations of the area A correspond positively with the pressure but the mean value itself first decreased until about 80 kPa before beginning to increase again. The mass shows two outliers at 55 kPa and 70 kPa and seems to be randomly distributed whereby a slight correlation in between mass and area could be suspected. Nonetheless, the overall behaviour of area and mean dot mass as a function the piston-pressure and therefore momentum transfer cannot be explained.
The same applies to the cartridge-pressure. A clear positive (and possibly linear within error intervals) correlation with the area is observed. The mean dot mass, however, seems to decrease. A possible spillage of glue, pressed out of the nozzle for high pressures without a movement of the piston, would slightly increase the mean dot weight compared to the initial parameter value (the opposite of the observed, comparing dot masses for all three parameters varied) but especially lower the momentum of the whole glue dot, because only a fraction of the dot gets actually accelerated and has to carry the spillage off (accelerate it).

Despite some unpredicted correlations, respectively the lack of these, the glue tests described above gave a good overview of the possibility to dispense the single component epoxy resin *DYMAX® Multi-Cure® 6-621*. While no lines and only some satellites of category 2 occurred, there was a medium number satellites of category 1 compared to previous tests with *Strucalit® 3060 N*. However, several parameter sets near the initial set show none or negligible satellite numbers as well as generally good shapes (circles instead of ellipses). The small statistical fluctuations in the half-axes ratio seems to be negligible.
Further research has to be conducted on the area A and its correspondence with the parameters on the one hand, and the other quantities (especially mean dot mass) on the other. Secondly the area - cartridge-pressure correlation needs to be explained.
In general the initial parameters seem to be good enough (no better were observed) to be used for further glue tests. These tests will have to determine the number and exact position of the glue dots as well as the maximal force it can sustain before braking off to guarantee safe, durable and thermal expansion resistant detector strip modules.

4. Precision measurements and calibration

Before the real HV-MAPS can be glued onto the polyimide strips, the overall precision of the glueing robot has to be determined. This especially includes the flatness and orientation of the granite slab (bed) in three-dimensional space. In section 4.1 different measurement methods for the flatness are developed, described and their results evaluated. Section 4.2 deals with the angle in between the x- and y-axis.

4.1. Flatness of the granite slab

The granite slab used as a bed has been manufactured with a defined flatness of less than 2 µm from its mean [3]. However, it is loosely mounted onto the aluminium structure with four rubber studs and held in place solely by its weight of 25 kg. Because the granite slab is 5 cm thick and made of solid, stable stone any deflection due to its own weight or any reasonable mass laid on top of the slab are negligible. Hence, the aluminium structure as well as the deflections of the x- and y-axis of the robot remain as main error sources for a non-constant distance in between the z-axis (at position z) and the surface. A constant distance is however necessary to achieve a precise placement of glue and the only 50 µm thick HV-MAPS, especially because the latter are pressure sensitive and must not be squeezed.

It is assumed that in particular the y-axis suffers at least a small deflection caused by the weight (z-axis with payload) placed at its end. Furthermore, this deflection should be positively correlated to the y-position because a larger outreach leads to a longer lever and therefore higher torque. On the other hand, any force exerted by the z-axis leads to a counteracting torque which may overcompensate the first one.

In the following two different methods to measure the distance between the z-axis and the granite slab are described, executed and analysed. Method 1 uses the built-in feature of the motors to measure currents and therefore forces while method 2 relies on an external dial indicator screwed onto the structure.

4.1.1. Method 1 - usage of Drive I_Force

The current I supplied to the LINAX® and ROTAX® axes is directly proportional to the force or torque the motor exerts. The motor controller offers the possibility to define upper limits on the force as well as commands which lead to conditional movements whereby *error 30* [4, p. 112] is thrown if the maximal force is reached (exceeded). Firstly, it is possible to define a global force maximum in the *I_FORCE LIMITATION* column of the *move axis - by Forceteq®* tab which is rather a limitation serving operational safety. Secondly, the controller offers the possibility to define up to 10 *Drive I_Force* profiles in the *application - drive i_force* tab consisting of an acceleration, target speed, maximal force and direction of movement (in- or decreasing increments, so down or up in case of the z-axis). The smoothing factor is a global parameter and copied from the *move axis - by click* tab. [4, p. 61]

Using the command *DIFx* the motor will move with the parameters set in the x-th *Drive I_Force* until the maximal defined force is reached and stop in the final position, further exerting this force, so it has to be stopped (e. g.via *Stop Motion* - *SM*) and *error 30* cleared before being moved again.

The distance in between the z-axis and the granite slab can now easily be determined by commanding the z-axis to move downwards with a *Drive I_Force* command until the r-axis rotor hits the slab.

To minimise a possible influence of the momentum transfer (which directly depends on the speed the slab is hit) the speed is kept small. The start position of the movement as well as the acceleration must then be chosen in such a way that the axis has reached and stabilised its target speed upon hitting the stone. Furthermore, each measurement must be completed within 8 s because of limitations of the build-in measuring tool (tab *move axis - by Forceteq®*).

In order to investigate the supposed behavior and because WebMotion® offers an easy possibility to retrieve and save all desired data (comparable to section 3.2.2)[1], a *Drive I_Force* profile was implemented with the following parameters:

$$z = 76 \times 10^3\,\mathrm{Inc} \qquad s = 100\,\% \qquad a = 100 \times 10^3\,\mathrm{Inc\,s^{-2}} \qquad v = 500\,\mathrm{Inc\,s^{-1}} \qquad F = 9.5\,\mathrm{N}$$

The acceleration a is large enough (even though s is maximal) that the axis reaches its target speed in less than 1 s while the start position z is far enough away from the slab (approximately at 80×10^3 Inc) to give enough space for a constant motion as well as not being too long to exceed the maximal 8 s measuring time. The requirements stated above are therefore met.
For each measurement the z-axis was first put into the starting position z by using the *Go Position* entry in the *move axis - by click* tab and then commanded to drive into positive direction (increasing position, motor moves downwards) as well as starting a new measurement via *Drive I_Force* by using the commando *DIFx*, whereby x is the number of the appropriate *Drive I_Force* profile.
Because the y-axis is thought to have the most influence on the actually measured final position, it was decided to take all data with $x = 130 \times 10^3$ Inc (oriented to the measuring positions of the inspection report of the slab [3]) but different, nearly equally spaced, y-positions 0 Inc, 43×10^3 Inc, 86×10^3 Inc, 130×10^3 Inc, 173×10^3 Inc, 216×10^3 Inc, 303×10^3 Inc and 320×10^3 Inc. For every y-position the z-axis was driven 15 times onto the granite slab. Figure 4.1 shows exemplary all 15 measurements taken at $y = 216 \times 10^3$ Inc as a function of absolute position.

[1] Measurements within this section have been done with *Forceteq®* in the *move axis - by Forceteq®* tab, however this is equal to the measuring process used to archive data in the *move axis - motion diagram* tab.

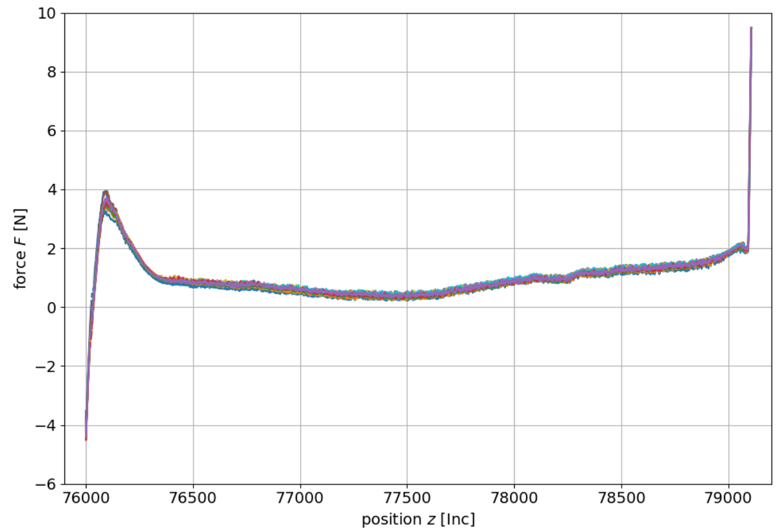

Figure 4.1.: Force as function of absolute position for all 15 measurements at y-position 216×10^3 Inc. A legend has been omitted for reasons of readability, each graph (colour) corresponds to one measurement.

The general course of the graphs in figure 4.1 can be divided into three sections. During the first one from 76×10^3 Inc to 76.5×10^3 Inc the motor accelerates to its target speed, momentarily applying a high current to get the inert mass moving. After having accomplished this a long route of steady motion follows before an abrupt deceleration when hitting the granite slab. The second section starts at about 76.5×10^3 Inc and ends right in front of the sudden rise at about 79.1×10^3 Inc. The force applied is relatively small in contrast to the first and last section but not really constant as one would expect, ranging in between 0.2 N and 2 N. The de- and increasing cannot be explained and is thought to be caused by the specific setup. Finally the third section starts at approximately 79.1×10^3 Inc and contains the sudden rise when the shaft of the r-axis hits the granite slab and the motor has to counteract the resistance followed up. Especially note the small dip just in front of the rise. The dip, as well as the u-shaped behaviour in section two, is consistently present throughout all measurements and all y-positions. It is thought to be caused by the specific settings (speed, smoothing factor, acceleration) used. Further investigation, however, would not bring any new insights concerning this thesis and may be conducted in the future [9].

For each y-position the mean of all 15 measurements was taken, figure 4.2 shows a closeup of the third section (the section of interest) of the corresponding force profiles as a function of absolute position. Note the different slopes as well as start positions of the final rise.
All nine curves show a more (lower values of y) or less (higher values of y) specific level-off characteristic at the final maximal force $F = 9.5$ N which results from the trigger of *Drive I_Force*. It takes some time for the motor control to measure the maximal allowed current (force) and stop movement as well as data acquisition. Furthermore, the red curve shall be pointed out because of its smaller slope compared to surrounding violet and brown curves.

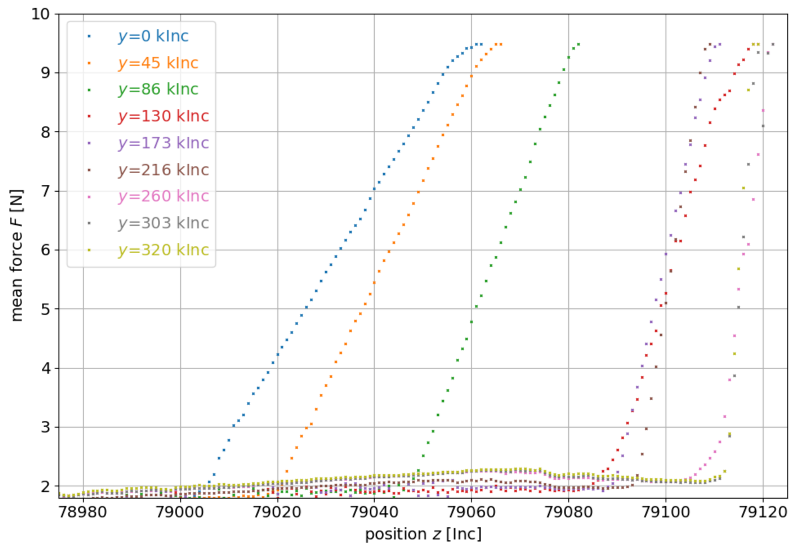

Figure 4.2.: Force $F(z)$ exerted by the z-axis s a function of absolute position averaged over all 15 measurements for all 9 y-positions.

To analyse the coherence in between final position z_F and force F exerted by the z-axis, z_F is determined numerically and defined as $z_F := \min\{z|F(z) \geq F\}$ with the canonical uncertainty of $\Delta z_{F-} := \max\{z|F(z) \leq F - \sigma\}$ and $\Delta z_{F+} := \min\{z|F(z) \geq F + \sigma\}$, respectively, whereby σ is given by the standard deviation of $F(z_F)$ which results from the averaging process of all 15 measurements. For some y-positions the results as well as a linear fit are shown exemplarily in figure 4.3, all data is presented in appendix E.

Before discussing the main results it must be stated that the very first data point ($F = 2\,\mathrm{N}$) has not been included into the fit. Note that there is no theoretical model of the expected behaviour but rather an a posteriori justification of the linear dependence, concluded from the present distribution. The first data point clearly differs from a linear relationship which can be concluded from figure 4.2: A horizontal line at $2\,\mathrm{N}$ would not intersect the quickly rising part of the graphs but rather the still flat section just before the rise.
Secondly, even though error bars are generally small, especially measurements at $y = 260 \times 10^3\,\mathrm{Inc}$ and $y = 320 \times 10^3\,\mathrm{Inc}$ contain significantly larger error bars which directly result from data (statistical error). Even though the affected datapoints correspond to small forces and the rather low accuracy of $0.25\,\mathrm{N}$ is assumed to have a significant impact there is no plausible explanation what could have caused the differences from the other measurements. All parameters were constant for all data presented, furthermore, the data has been taken continuously on the same day within several hours. An influence of temperature or weight compensation pressure can therefore be ruled out. Despite the large error bars the data points fit in the linear model very well.

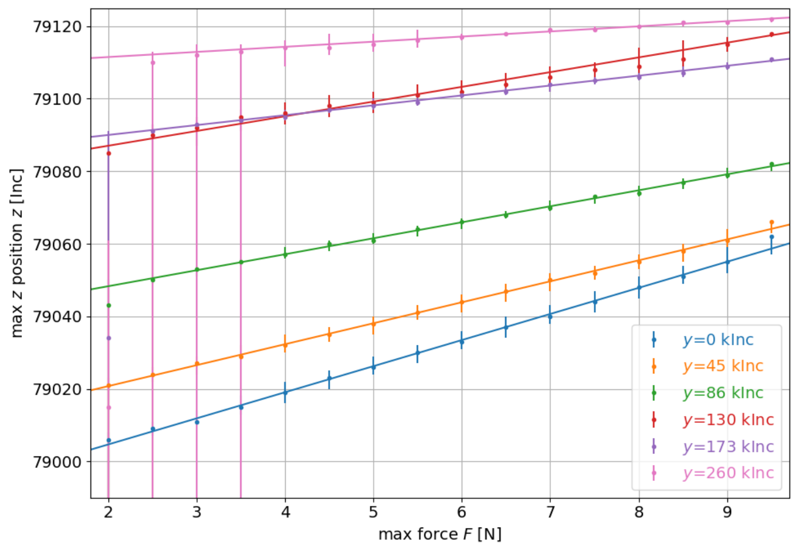

(a) Absolute position z_F with linear fits over all but the first ($F = 2\,\mathrm{N}$) data point.

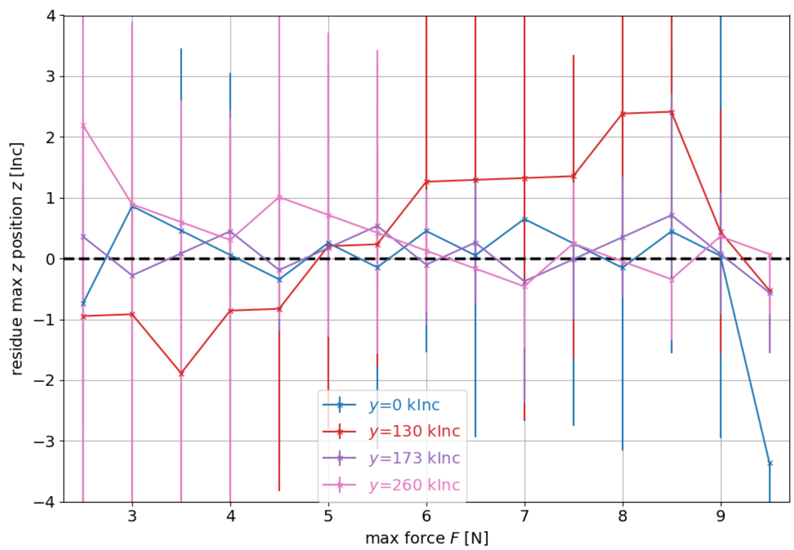

(b) Residual plot of some of the linear fits shown in figure 4.3a.

Figure 4.3.: Absolute position z_F of the z-axis while exerting force F. Exemplary data shown for some y-positions, all data see section E.

To additionally justify the linear fits, a residual plot of some of the data sets plotted in figure 4.3a is shown in figure 4.3b (all data is presented in appendix E). The residuals of the blue and pink data sets stay well within ± 1 Inc, only red exhibits a larger interval (± 2.5 Inc) and features a much more systematic shape. However, these deviations from all other sets

cannot be explained and run through the following analysis. Note that the errors (except the first four of the pink measurement) stay well within a relatively small interval of only ± 5 Inc which furthermore stresses the linear coherence.
Finally the large deviation (sudden drop) at $F = 9.5\,\mathrm{N}$ can be seen for all nine different y measurements. It is indeed systematic and results from the absolute maximal force the motor controller was limited to. They correspond to the level off characteristic described above (also see figure 4.2).

The nine different y-positions (in the following uniquely identified by their colour) can visually be split into three groups of three, firstly the lower three (blue, orange and green), secondly the middle group (red, violet and brown) and lastly the uppermost in mustard, grey and pink (see appendix E). Note that this sequence corresponds with the y-positions in increasing order, so decreasing length of the lever.

Finally, figure 4.3a shows the following correlations:

1. The slope of the linear fit decreases in groups with increasing y-position (with the exception of red) but with significant differences in group one. So with decreasing lever length, less additional distance Δz can be achieved with the same additional force ΔF (slope $m := \frac{\Delta z}{\Delta F}$) which perfectly corresponds to the decreasing lever length: The longer the lever, the greater the torque a constant force at its end will generate and the greater the deflection of the y-axis.
   However, this is no explanation for the above grouping as well as the behaviour of red because a consistently declining slope over all nine individual y-positions is expected.
2. The most obvious feature to be seen is the positive correlation between force and absolute position (all slopes are positive). The more force is exerted the further down the z-axis can move or the higher the motor rail pushes itself up while bending the y-axis rail.
3. The y-axis intercept of the fitted curves correlates group wise, and within group one individually, with the y-position. This, however, cannot be explained by an in- or decreasing lever length but rather a not perfectly even surface and is the quantity to be measured. For further analysis on the significance of these values see below and section 4.1.2.

For better visualization figure 4.4 shows the slopes of the fitted linear functions shown in figure 4.3a as a function of y-position. The uncertainty in y was set to less than 12 Inc as stated in table 2.1 and cannot be seen hence. The uncertainty in the slope itself was determined by the fitting method and mainly correlates with the statistical uncertainties propagated. A clear negative correlation between slope and y-position can be seen, however the functional dependence is not easy to extract. Note that the data point at $y = 130 \times 10^3$ Inc is far off the other data, which corresponds to all the information gained above (130×10^3 Inc corresponds to the red measurement of the second group). Because the cause of this behaviour is not understood but no systematic reason is expected the data point was excluded from any further analysis.

The structure of the y-axis is too complicated to be modelled theoretically so any function fitted would just be a guess. A linear dependence would be justified according to the data available and is shown in orange. However, especially the first two data points at low values of y (maximal lever length) differ clearly so a hyperbolic dependence could also be possible. Also note the rather large reduced chi squared of $\chi^2_{red} = 5.09$ which indicates a not well fitting fit. Lacking a reliable theoretical model no further investigation of the behavior has been taken into consideration.

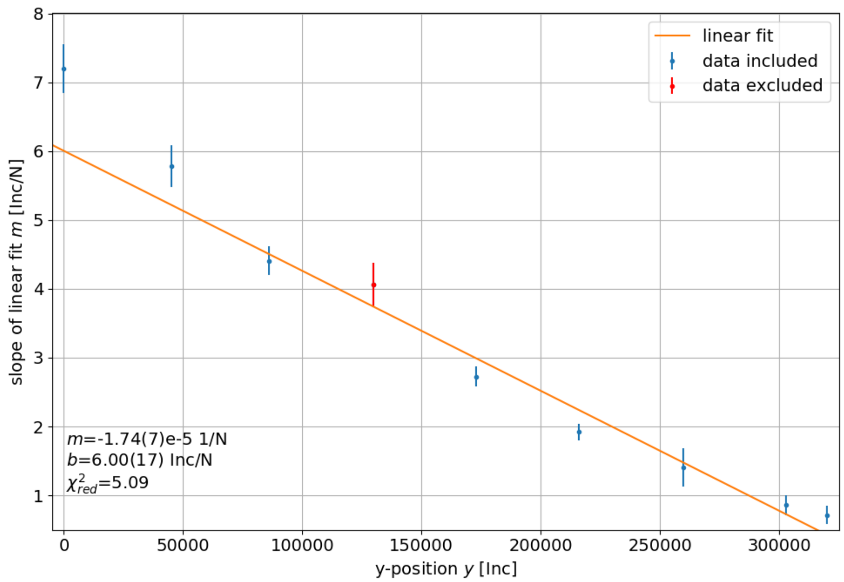

Figure 4.4.: Slope of the fitted linear function (see figure 4.3a) as a function of y-position. Data used for fitting in blue, excluded data in red and the linear fit in orange.

As the results discussed above have shown, the absolute distance in between z-axis and granite slab is positively correlated to the exerted force due to the bending of the y-axis. This makes it impossible to determine a force that shall be used for calibration measurements (i. e. not influencing the results due to bending). To further investigate at least the deviations of the absolute position a second method is needed (see section 4.1.2).

4.1.2. Method 2 - usage of an indicator

An alternative measurement technique using an indicator (resolution: 1 µm, range: 1 mm) instead of relying on the internal force measurement of the z-axis was proposed. The distance in between z-axis and granite slab is measured by pushing the tip of the measurement stamp onto the slab as shown in figure 4.5.

The indicator itself weights (78 ± 2) g, the black mounting stand (292 ± 2) g, so an additional weight of a little less than 400 g has somehow to be attached to the y- or z-axis in such a way that the indicator touches the granite while at the same time affecting the measurement itself as minimally as possible. The measurement is affected by the additional torque acting on the lever (y-axis) and bending it further than already done by the payload on the z-axis.

Note that no absolute distance can be determined this way. This would only be possible if the indicator value is directly linked with a motor position of the z-axis which is impossible without having a well-defined state (e. g. r-axis shaft resting on the granite).
Even though any torque caused by the indicator stays well within the motor limits (see section 3.1) and no upward bending of the y-axis is expected (r-axis shaft does not touch the granite slab, mechanical resistance of the indicator can be neglected) the first correlation described in section 4.1.1 is still present:
The larger weight (torque) leads to a larger bending of the y-axis for a long lever (small y-positions) and thus increases the relative distance differences depending on the y-position but independent of x. For practical matters, it was thus decided to mount the indicator directly upon the z-axis (see figure 4.5) instead of designing a holding structure which could have been fixated directly on the y-axis rail. The additional bending caused by the additional load is thought to play only an insignificant role.

Because of the inspection report [3] it is thought that the slab itself is flat in terms of deviations from the mean but rather tilted into an arbitrary direction. The deviations in the distance between z-axis and slab is therefore thought to be a plane, overlaid with a second plane whose normal vector is nearly parallel to an idealised z-axis but slightly tilted forward (to the front of the robot). This curved surface is caused by the bending of the y-axis, leading to smaller distances for longer lever length (smaller y-positions). The second plane is only a plane in first order approximation as the measurements in section 4.1.1 have shown. With smaller lever length, the differences in between the fitted linear function became smaller. Note that this effect is thought to be small in comparison to the (yet unknown) tilting of the slab.

In order to gather measurement data the z-axis (with attached indicator is driven from a start position z_1 towards a constant final position z_2. The start position z_1 is rather arbitrary but shall not be too small (position of the motor too far up) for practical matters: The larger the distance $\Delta Z \coloneqq z_2 - z_1$ the longer each single measurement takes (target speed is constant). The final position z_2 shall be constant for all positions (x, y) to eliminate any possible systematic error. Secondly it must be chosen in such a way that the r-axis shaft never hits the granite while at the same time being close enough to the surface, so the indicator is within measurement range of only 1 mm.
Speed, acceleration and smoothing factor should not play any significant role if kept within reasonable limits (large acceleration or target speed lead to strong vibrations which could in fact affect the results). To further eliminate any systematic differences between method 1 and 2 these parameters were kept constant. Finally, the parameters were set as follows:

$$z_1 = 76 \times 10^3\,\mathrm{Inc} \qquad z_2 = 78.6 \times 10^3\,\mathrm{Inc}$$
$$s = 100\,\% \qquad a = 100 \times 10^3\,\mathrm{Inc\,s^{-2}} \qquad v = 500\,\mathrm{Inc\,s^{-1}}$$

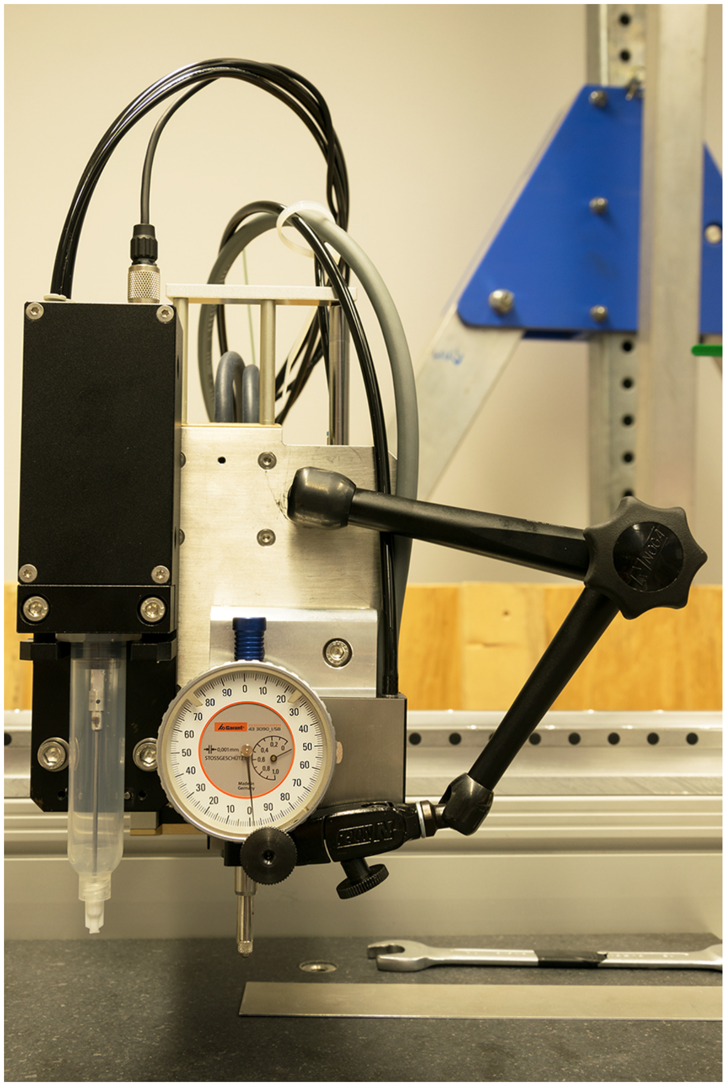

Figure 4.5.: Indicator mounted onto the z-axis so that the measuring stamp is located (20 ± 2) mm in front of the r-axis shaft.

A C++ programme was written to drive the z-axis periodically up and down between z_1 and z_2, remaining in position z_2 until the user commands it upwards again with the help of an input signal. In the meantime the indicator can be read off. To gather enough data the procedure was repeated 20 times for every (x, y) position desired. To achieve a wide and uniform coverage of the entire slab the measurement points were chosen to be equal to the ones used in the inspection report [3]: The 40 cm × 40 cm slab can easily be covered by a grid with 13 cm side length, leading to 16 positions in total. Note however, that due to the construction of the robot the last row (maximal y-position at minimal lever length) is only 6 cm instead of 13 cm apart from the one before (also see figure 4.7) which should not affect the measurement.

Finally, all 20 values per (x, y) position were averaged and plotted as a function of position as shown in figure 4.7 in blue. An arbitrary reference point of $(x = 0\,\text{Inc}, y = 320 \times 10^3\,\text{Inc})$ was used. The green surface shown in figure 4.7 is a fit of a perfectly flat plane for visualization purposes.
The systematic errors of the indicator are small, the mounting is very rigid so it is not assumed to be moved under the influence of the tiny force the tip exerts onto the slab. Furthermore, the resolution of $1\,\mu\text{m}\,\text{DIV}^{-1}$ enables a small readout error of $0.5\,\mu\text{m}$. The total uncertainty on the averaged indicator position is given by $\Delta z_{tot} := \sqrt{\Delta z_{sys}^2 + \Delta z_{stat}^2}$ with the just defined systematic uncertainty Δz_{sys} and the statistical Δz_{stat}, respectively. Note that both contribute nearly equally (see statistical uncertainties in figure 4.6).

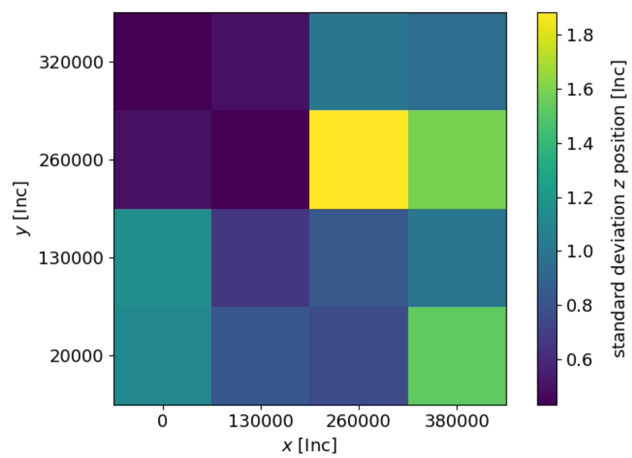

Figure 4.6.: Standard deviation of the difference in distance in between z-axis and granite slab as a function of the 16 (x, y) positions.

The measured results clearly differ from the expected shape:
The fitted green plane shows a significant tilt in the x-direction but only a minor, insignificant one in the y-direction, which would only be explained by tilting the whole slab but not by bending the y-axis. Comparing measured and fitted values they clearly differ the most (by about 200 Inc) at the left front as well as right rear corner, leaving the measured surface appear not only tilted but rather curved with a large radius. This curvature cannot be explained with the model described above. The granite slab itself is too rigid to be curved by its own weight and the fact that it rests on four rubber studs in such a significant way. Furthermore, the bending of the y-axis (which should be equal for all x-positions) cannot be observed. According to the model the deviation should be smaller for large y-positions (small lever length) and decrease towards the front of the robot with absolute differences in the order of a few 10 Inc. As figure 4.7 clearly shows, this is qualitatively the case for $x = 260 \times 10^3\,\text{Inc}$ and $380 \times 10^3\,\text{Inc}$ but the other way around for $x = 0\,\text{Inc}$ and $130 \times 10^3\,\text{Inc}$. Quantitative differences are around 200 Inc for $x = 0\,\text{Inc}$ as well as $380 \times 10^3\,\text{Inc}$ and thus a magnitude larger than expected.

A comparison with the results from method 1 is only possible for one x-position ($x = 130 \times 10^3\,\text{Inc}$): The difference in the distance d in between the z-axis and the granite slab for the two most extreme y-positions ($y_1 = 0\,\text{Inc}$ - longest lever length, $y_2 = 320 \times 10^3\,\text{Inc}$ - shortest lever length) is about 80 Inc (80 µm) and can roughly be interpolated linearly in between. Thereby is d positively correlated with the y-position.

Method 1 does indeed show the same results: With growing y-position y the distance d gets larger (see figure 4.3a). This difference in d is quantitatively heavily influenced by the maximal force exerted. From $F_1 = 2\,\mathrm{N}$ to $F_2 = 9.5\,\mathrm{N}$ the difference in distance d concerning the most extreme y-positions (y_1 and y_2) decreases linearly from about 105 Inc (105 µm) to only 60 Inc (60 µm), respectively.
So within uncertainties and the influence of the force exerted in method 1 both techniques show qualitatively and quantitatively the same result. Even though both cannot be used to determine the bed-leveling as originally desired.

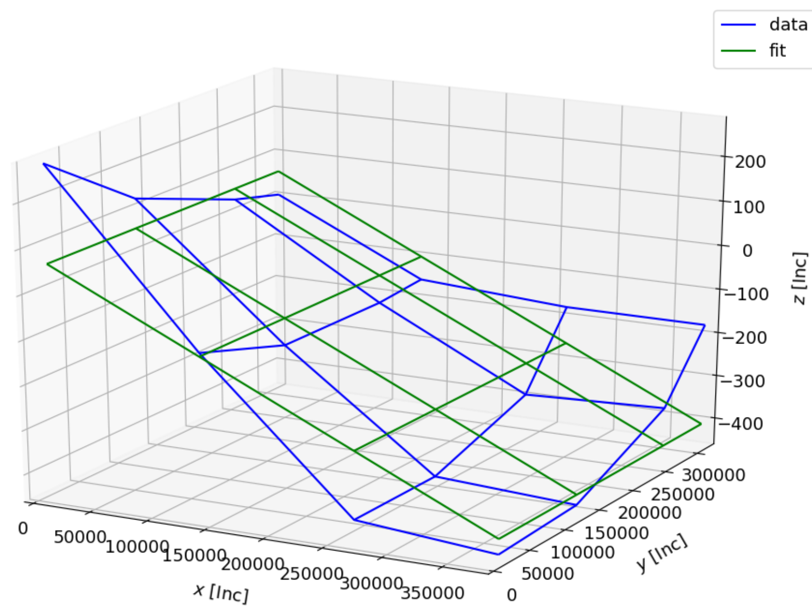

Figure 4.7.: Difference in distance in between z-axis and granite slab as a function of (x, y) position. Data in blue, plain fit for visualization purposes in green.

4.1.3. Comparison and outlook

Two different methods have been used to measure the distance between the z-axis and the granite slab. While the first one used the capabilities of the axis itself (internal current and therefore force measurement), did the second one rely on an external indicator screwed onto the apparatus.
Method 1 produces values suiting the imposed model quite well but the results cannot be used to answer the original question (bed leveling) due to the bending of the y-axis. It is also thought to be less precise because of the rough resolution of only 0.25 N.
Method 2 is a generally accepted and widely used technique for bed-leveling in industry as well as consumer used 3d-printer and CNC machines which require a high precision and therefore expected to be very precise. However, it is only a relative measurement so the absolute position of the z-axis with respect to the granite slab is still unknown.
All in all, the bed-leveling is much more complicated than initially thought. To further investigate the distance between z-axis and granite slab the influence of any external equip-

ment should be reduced (less weight leads to less torque) as well as automatised for practical reasons. Purchasing a laser distance sensor with a resolution of less than 10 µm (equivalent to 10 Inc) and readout possibility would be a third and radically new approach, meeting the above stated requirements.

4.2. Perpendicularity x-y-axes

When picking up or placing HV-MAPS the motor control units of the x- and y-axis will be commanded to move their axis to a specific location. To guarantee a high precision placement of the HV-MAPS the axes must include a constant (preferably right) angle over all (x, y)-positions. In the following an easy and cheap method to determine this angle will be described, executed and analysed.

Because no specific analyse tools typically used for multi-axes CNC or 3D-printing machines were available, a method based on the 'Bi-axial straightness test' [2] was chosen, making use of an indicator as well as a square with a short side length of 20 cm and a long side length of 30 cm, respectively. The square has been manufactured according to the DIN 875/00 standards with a maximal deviation of 12 µm per 1 m side length [13].
As shown in figure 4.8, the square is clamped to the x-axis with the help of a screw clamp, having contact with the axis just below the rail the sled moves onto. Because the axes themselves are high precision instruments it is assumed that there sides are perfectly flat. To minimise the torque the clamp as to counteract, an aluminium support structure was constructed which holds most of the weight. The indicator is, just like in section 4.1.2, mounted to the z-axis so that its measuring stamp touches the edge of the square for a constant position of the z-axis. The latter can be chosen in a wide range because the stand of the indicator is freely movable. However, to minimise torque on the y-axis and guarantee a maximal measuring range (movement of the y-axis) the following x- and z-positions were chosen:

$$x_1 = 300 \times 10^3\,\mathrm{Inc} \qquad x_2 = 100 \times 10^3\,\mathrm{Inc} \qquad z = 69 \times 10^3\,\mathrm{Inc}$$

which results in a measuring range (range the y-axis can be moved with the indicator still touching the square) of 160×10^3 Inc to 320×10^3 Inc, or 16 cm in total. Note that x_1 belongs to the situation shown in figure 4.8 where the shorter leg of the square touches the left rubber stopper (x-position 0 Inc) whereas x_2 is used if the square is clamped at the other side of the x-axis (x-position 400×10^3 Inc). Other x-positions, taking the limitations of the shorter leg of the square into account, are in principal possible however, hardly reproducible lacking a fence (i. e. the rubber stoppers). The actual measurement is conducted by moving the y-axis back and forth in between $y_1 = 160 \times 10^3$ Inc and $y_2 = 320 \times 10^3$ Inc while monitoring the position shown by the indicator.

There are several reasons for the axes not to be perpendicular:

1. The y-axis sled is mounted onto the sled of the x-axis with 4 screws. This screw connection is thought to be the main error source but constant for all x- or y-positions and easy to be fixed by loosening the screws, varying the position of the y-axis a bit and fixing them again.

2. Both the x- and the y-axis are no perfectly straight but twisted due to manufacturing accuracy.
3. The moving part of the axis (x-axis: sled, y-axis: rail) may rotate around an arbitrary axis dependent on its position due to constructional limits to reduce backlash.
4. The x-axis may have been twisted in any arbitrary way whilst being mounted with the help of about 20 screws onto the main aluminium structure.

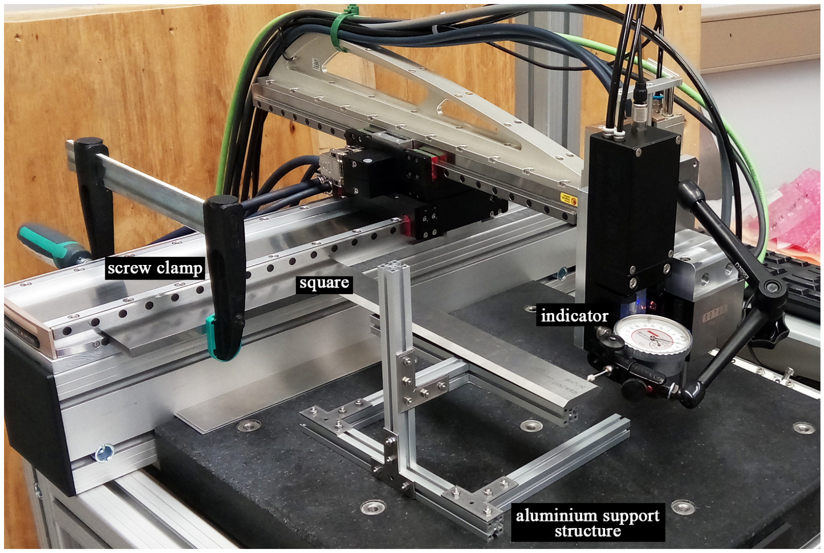

Figure 4.8.: Indicator mounted to the z-axis so that the measuring stamp touches the edge of the square attached to the x-axis with the help of a screw clamp.

While the first two effects cannot be quantified individually, there is an upper bound given for the sum of the latter two as they will not be separable in the final measurement. The twisting error of the x-axis is given by $QZ_x = 15''$ [6, p. 30] and $QZ_y = 35''$ [6, p. 22] for the y-axis respectively.
By assuming the x-axis to be perfectly flat (no torsion) and neglecting any torsion of the y-axis rail, because they cannot be corrected either way, the measuring technique described above makes any deviation from a right angle visible as a non constant distance in between the y-axis and the square.
Any distance variations in between granite slab and z-axis due to weight force implied torque on the x-y-connection was found to be too small to have any influence on the measurement, the tip of the indicator always stayed on the edge of the square.

Error source 1 can be corrected mechanically to guarantee the best possible setup. To achieve this a measurement in position $x = x_1$ is conducted, the four screws holding the y-axis in place are then loosened and the axis is turned to either side needed (until the distance in between y-axis and square is constant for all y-positions) by applying small hits with a hammer or hand. Finally, the screws are carefully fixed again. Note, that fixing the screws may have an effect on the angle, if so, the process must be repeated.

A second measurement in position x_2 follows to determine the severity of the remaining angle error $\Delta\alpha_{new}(x_2)$ according to:

$$\Delta\alpha_{new}(x) = \Delta\alpha_{old}(x) - \Delta\alpha_1 - (\Delta\alpha_2(x_1) + \Delta\alpha_3(x_1) + \Delta\alpha_4(x_1))$$

This remaining error at any x-position x results from the angle error before correcting the y-axis position ($\Delta\alpha_{old}(x)$), the - now eliminated - constant error $\Delta\alpha_1$ (1) and the overcompensated effects of the twisted axes (2), backlash (3) and the mounting of the x-axis (4).
Because reason 1 is thought to be the leading factor $\Delta\alpha_{new}(x)$ should be smaller than $\Delta\alpha_{old}(x)$ for all x. Further improvement should be achievable by varying the force applied to the x-axis by the screws holding it onto the robot structure.

The above strategy has been conducted by the author together with the engineer who constructed and built the glueing robot (Peter Bernhard). The first measurement in position x_1 showed a distance variation of about 80 µm between square and y-axis in between y_1 and y_2 which could be eliminated by loosening the four screws of the y-axis. However, fixing them again lead to a distance variation of about 23 µm at $y = 160 \times 10^3$ Inc (about $8''$) which could not be eliminated despite several attempts. A measurement at x_2 revealed a similar variation of about 34 µm at $y = 160 \times 10^3$ Inc (about $12''$).
Neither of them could be further reduced by the four screws of the y-axis nor the 20 screws of the x-axis, however, the deviations can be reproduced very well within the systematic read-off error of the indicator of 1 µm and the uncertainty of the square for both x-positions. This holds true for moving the y-axis back and forth as well as dismantling and reattaching the square. The latter proves that the placement of the square by using the rubber stoppers is fences is precise.

Figure 4.9 shows the distance deviation depending on the y-position with an arbitrary deviation of 0 µm at $y = 320 \times 10^3$ Inc (y-axis completely retracted). A linear regression has been applied to the data for better visualisation. Lacking a theoretical model of the axes torsion (there are too may variables to be taken into account) no quantitative analysis of the results will follow. Nonetheless figure 4.10 shows the residual plots.

Qualitatively the linear regressions lie within all errorbars so the angle error (deviation from right angle in between x- and y-axis) is constant in good approximation but not vanishing for all y-positions, even though it clearly depends on the x-position. Nonetheless and with unknown cause, a sine with an amplitude of 1 µm to 2 µm is modulated onto the linear relationship as clearly shown by the residual plots. The sine could be caused by the axis design (axis are moved with the help of electromagnets placed in constant distance to each other) or the measuring itself (measuring stamp of the indicator glides over the hairline of the square as both are not aligned vertically) but because of its very small amplitude it is believed to be negligible for the final placement accuracy of the HV-MAPS (deviation from target position smaller than 100 µm) and has therefore not been investigated any further.

All in all with the method described above, it was not possible to establish a right angle in between x- and y-axis for all (x, y)-positions but rather a reduction of the angle error by eliminating the main error source (y-axis mounting). The remaining angle error was found

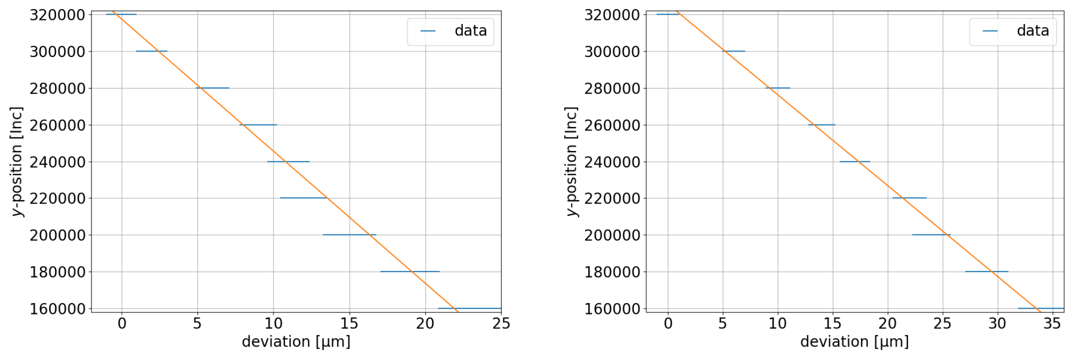

(a) $x = x_1 = 300 \times 10^3$ Inc.

(b) $x = x_2 = 100 \times 10^3$ Inc.

Figure 4.9.: Distance differences in between y-axis and square as measured by the indicator (see figure 4.8 for setup). Data in blue, linear regression in orange.

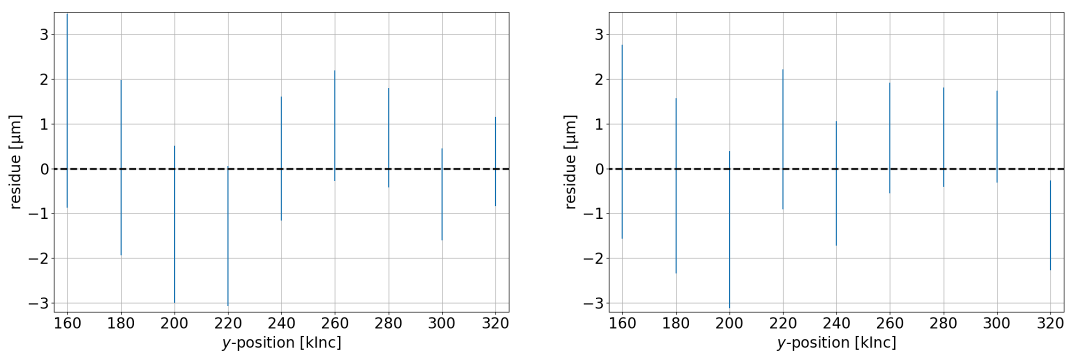

(a) $x = x_1 = 300 \times 10^3$ Inc.

(b) $x = x_2 = 100 \times 10^3$ Inc.

Figure 4.10.: Residual plot of the linear fits shown in figure 4.9.

to be dependent on the x-position but with good approximation invariant of the y-position. The method is easy to use but somehow limited when it comes to the number of possible measurement positions because of the need of a fence (rubber stoppers) and side length of the square. Both limitation can be evaded with the help of multiple squares with different side length ratios.
A further reduction of the angle error by mechanical manipulation of the setup is questionable because of the multiple error sources which cannot be distinguished and the multiple variables (screws). It is easier to calibrate the angle error out by correcting the target position with the help of the C++ script used to control the axes. Data needed for this approach could be acquired by a laser distance sensor mounted on the z-axis (compare to 4.1.3) and two fences parallel to the x- and y-axis placed alongside the edges of the granite slab. This approach would also have the advantage of an absolute measurement, taking the position of the granite slab (where the HV-MAPS will lie) into account.

List of Figures

1.1. Setup of the P2 experiment [8]. 5
1.2. Strip module of the tracking detector. 6

2.1. Close-up of the working surface with all four axes and the glue dispenser. . . 7
2.2. Overview of the glueing robot. 8
2.3. Forces and torques on a LINAX® linear motor [6, p. 24]. 10
2.4. Force and resulting torque acting on the y-axis sled. 11
2.5. Close-up of the electronic and computer space below the granite slab. 13
2.6. Glue dispensing unit *SG-JE 100*. 14
2.7. Glue dispenser control device *Jet DISPENSER JDC-200H*. 15
2.8. Tip of a ceramic nozzle. 15

3.1. Deviation from target position. 19
3.2. Exemplary force profiles F_{Pi} for every pressure P applied. 23
3.3. Force exerted by the z-axis for different weight compensation pressures. . . . 24
3.4. Exemplary evaluation standards (circle and ellipse) for glue dots. 27
3.5. Exemplary statistics on glue dot properties under piston-pressure variation. . 29

4.1. Force profiles at $y = 216 \times 10^3$ Inc. 33
4.2. Force exerted by the z-axis on granite slab. 34
4.3. Exemplary z-position per force F. 35
4.4. Slope of final z-position as a function of y-position. 37
4.5. Indicator mounted onto the z-axis (distance measurement). 39
4.6. Standard deviation of the difference in distance in between z-axis and granite slab. 40
4.7. Difference in distance in between z-axis and granite slab. 41
4.8. Indicator mounted to the z-axis (angle measurement). 43
4.9. Distance differences in between y-axis and square. 45
4.10. Residual plot for linear fits shown in figure 4.9. 45

A.1. *move axis - by click* 50
A.2. *move axis - by Forceteq®* 50
A.3. *move axis - motion diagram* 51
A.4. *setup - state controller* 52

C.1. Glue dots evaluation standards. 56

D.1. Statistics on glue dot properties under piston-pressure variation. 57
D.2. Statistics on glue dot properties under on-time variation. 58
D.3. Statistics on glue dot properties under cartridge-pressure variation. 59

E.1. Absolute position z_F of the z-axis while exerting force F. 61

List of Tables

2.1. Key parameters LINAX® linear motors. 9
2.2. Key parameters ROTAX® rotary motor. 9

3.1. Indices defined to be used with the weight compensation test programme. . . 22

B.1. Parameter values LINAX® linear motors. 53
B.2. Parameter values ROTAX® rotary motor. 53

Bibliography

[1] Dominik Becker et al.
'The P2 experiment'.
In: *The European Physical Journal A* 54.11 (2018), pp. 1–61.

[2] M.A.V. Chapman.
Calibration of machine squareness.
Tech. rep. TE328.
Gloucestershire GL12 8JR, GB: Renishaw plc, May 2013.

[3] M. Fleischer.
Qualitätsprüfzertifikat.
Tech. rep. 234291-1.
PLANOLITH, Oct. 2020.

[4] Jenny Science AG.
Anleitung XENAX® Xvi 75v8 Kompakter Ethernet Servocontroller.
Jenny Science AG. Rain, Schweiz, 2020.

[5] Jenny Science AG.
Commissioning Checklist.
Jenny Science AG. Rain, Schweiz, 2020.

[6] Jenny Science AG.
Datenblatt LINAX®.
Jenny Science AG. Rain, Schweiz, 2018.

[7] Jenny Science AG.
Datenblatt ROTAX® Rxvp (vakuum pressure).
Jenny Science AG. Rain, Schweiz, 2020.

[8] Michail Kravchenko.
private communication.
2021.

[9] Marcel Mehr.
private communication.
2021.

[10] *Multi-Cure® 6-621.*
Tech. rep. E.
DYMAX® Corporation, June 2020.

[11] Luise Poley et al.
'Alternative glues for the production of ATLAS silicon strip modules for the Phase-II upgrade of the ATLAS Inner Detector'.
In: *Journal of Instrumentation* 11.05 (2016), P05017.

[12] *Technisches Datenblatt Strucalit® 3060 N.*
Tech. rep. 3.
Panacol-Elosol GmbH, Mar. 2020.

[13] THOME Präzision GmbH.
DIN 875 - Toleranz der Winkel.
`https://www.thome-praezision.de/deu/DIN875.html`.
accessed: 03.08.2021.
2021.

[14] Marco Zimmermann.
'Particle Rate Studies and Technical Design Development for the P2 Silicon Pixel Tracking Detector'.
PhD thesis. Johannes Gutenberg-Universität Mainz, 2019.

A. Screenshots WebMotion® web interface

The following screenshots show the most important tabs of the WebMotion® web interface offered by Jenny Science AG.

Figure A.1.: *move axis - by click*

Figure A.2.: *move axis - by Forceteq®*

Figure A.3.: *move axis - motion diagram*

(a) *setup - state controller - Basic*

(b) *setup - state controller - Advanced*

Figure A.4.: *setup - state controller*

B. Axes parameters

Table B.1 lists all parameters with their values of the three LINAX® linear motors as operative conditions were established according to section 3.1. The corresponding parameters of the ROTAX® rotative motor are shown in table B.2, respectively. Note that within this thesis the ROTAX® was not equipped with any payload yet, so no special set-up was required and hence no parameter deviates from its default value.
The default state is shown in brackets if it has been changed.

parameter name	x-axis	y-axis	z-axis
SLP-/ SLP+	0/ 400 000	0/ 320 000	0/ 80 000 (85 000)
Basic PAYLOAD	6000 (0)	4869 (0)	1439 (0)
Basic GAIN POS	30	34	25 (35)
Stability STAB-DYN	0	0	0
Deviation POS ACT	2000	2000	2000
Deviation TARGET	50	50	50
Avoid vibration notch FREQ	0	0	0
Avoid vibration active FREQ	256 (0)	0	0
Swing out reduction DAMPING	0	0	5 0
Swing out reduction FREQ	0.0	0.0	17.0 (0.0)

Table B.1.: Parameter values of all three LINAX® linear motors set up during the procedure described in section 3.1. Default values have been put in brackets if they have been changed.

parameter name	r-axis
SLP-/ SLP+	0/ 0
Basic INERTIA	0
Basic GAIN POS	100
Stability STAB-DYN	0
Deviation POS ACT	2000
Deviation TARGET	50
Avoid vibration notch FREQ	0
Avoid vibration active FREQ	0
Swing out reduction DAMPING	0
Swing out reduction FREQ	0.0

Table B.2.: Parameter values of the ROTAX® rotary motor. Because no set up according to section 3.1 was required yet the values are all default.

C. Evaluation standards glue dots

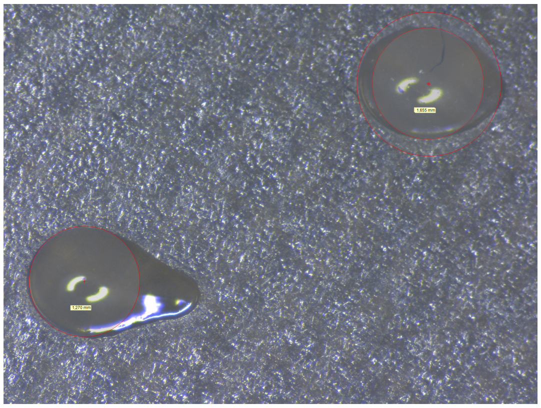

(a) Satellites of class 1 (both dots) - satellite still attached to the glue dot.

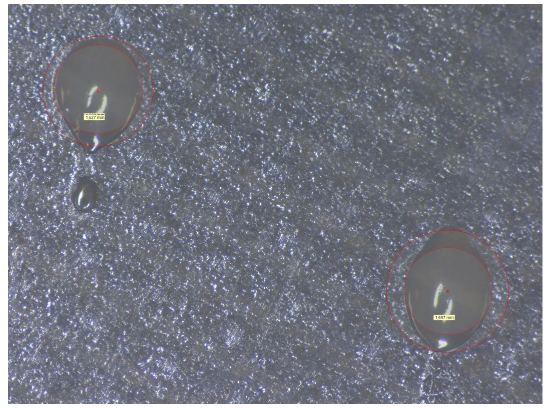

(b) Satellites of class 2 (left dot) - satellites separated from the glue dot.

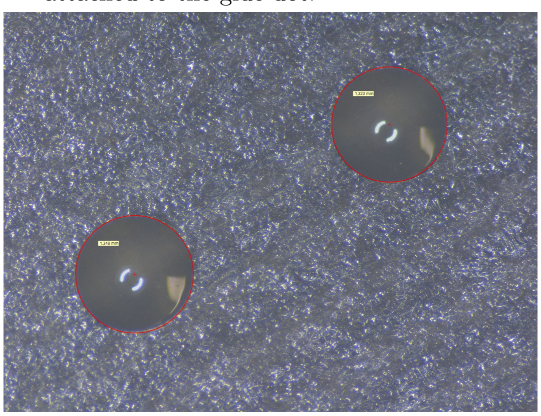

(c) Circles (both dots).

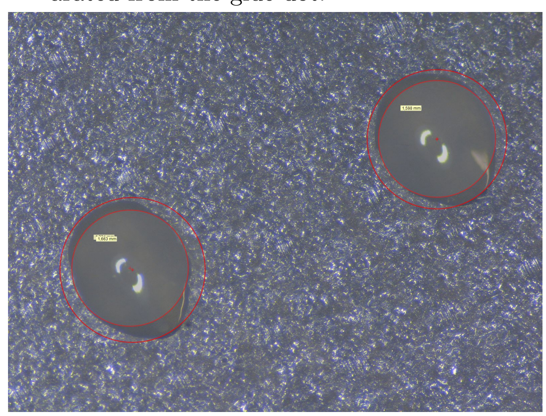

(d) Ellipses (both dots).

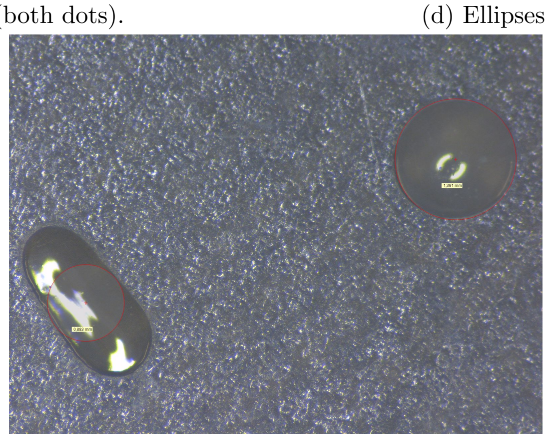

(e) Line (left dot).

Figure C.1.: Glue dots evaluation standards.

D. Statistics on dispensing parameters

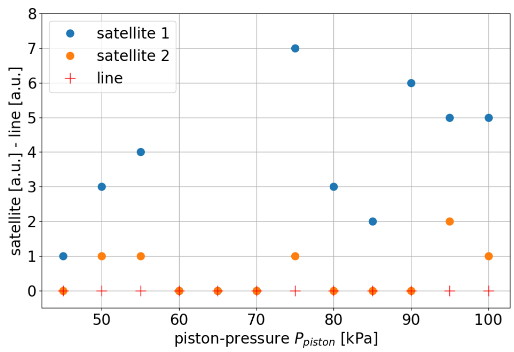

(a) Satellite and line number.

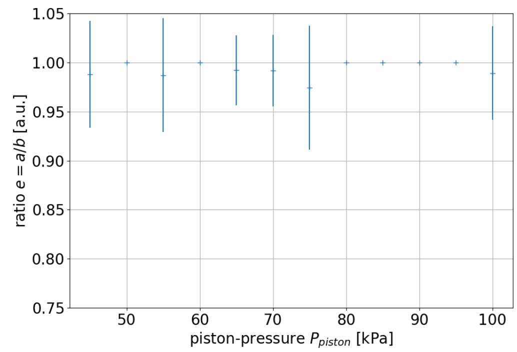

(b) Half-axes ratio $e \coloneqq \frac{a}{b}$.

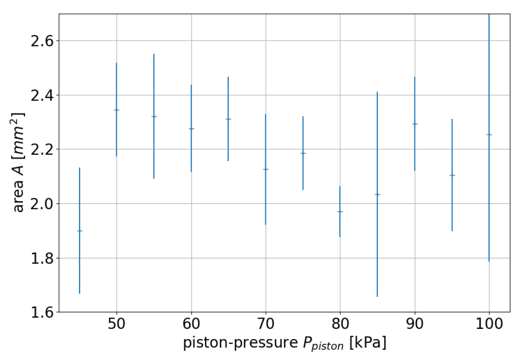

(c) Area A.

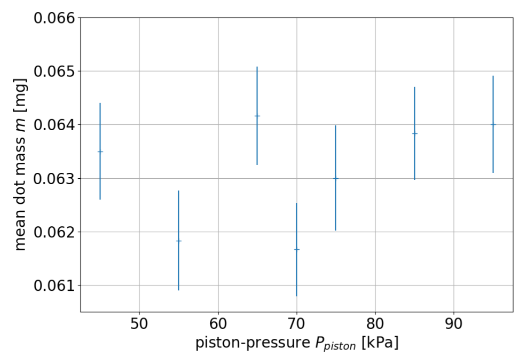

(d) Mean dot mass m.

Figure D.1.: Statistics on area A, half-axes ratio e, satellite and line number as well as mean mass m of the glue dots under variation of the piston-pressure P_{piston}.

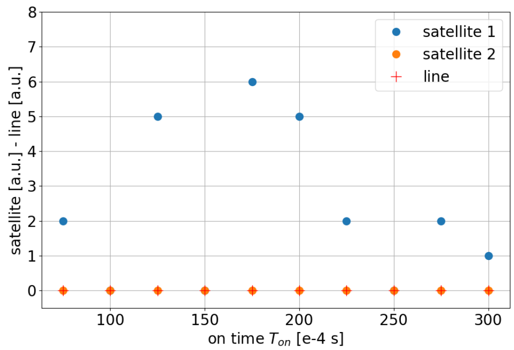

(a) Satellite and line number.

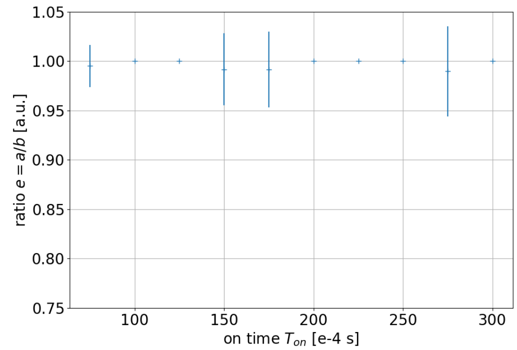

(b) Half-axes ratio $e \coloneqq \frac{a}{b}$.

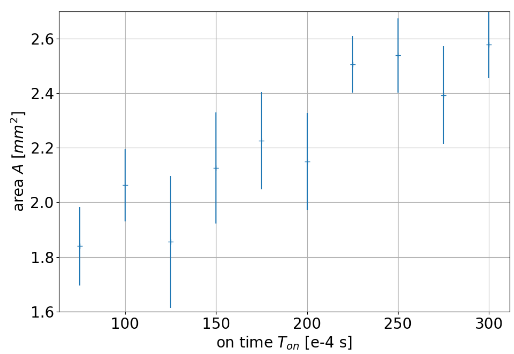

(c) Area A.

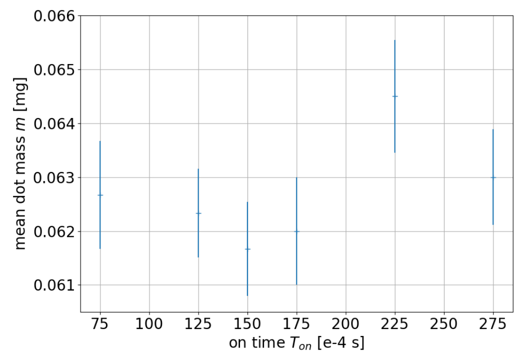

(d) Mean dot mass m.

Figure D.2.: Statistics on area A, half-axes ratio e, satellite and line number as well as mean mass m of the glue dots under variation of the on-time T_{on}.

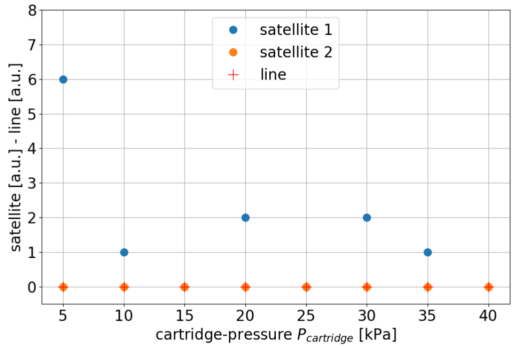

(a) Satellite and line number.

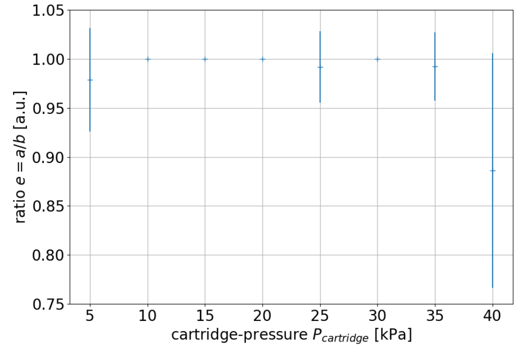

(b) Half-axes ratio $e := \frac{a}{b}$.

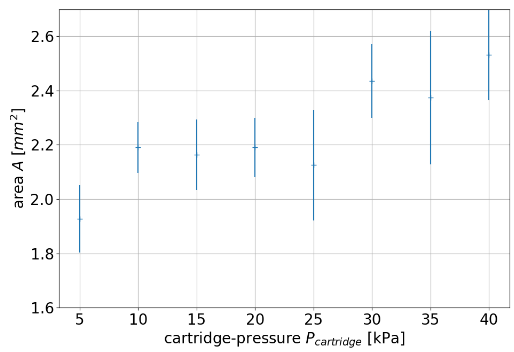

(c) Area A.

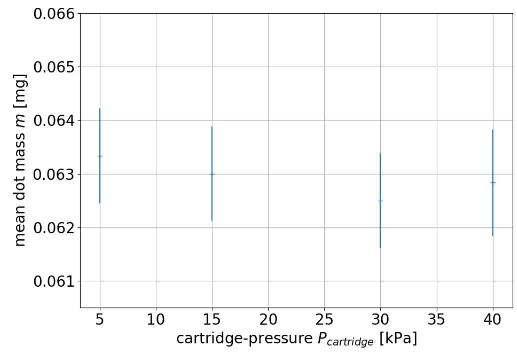

(d) Mean dot mass m.

Figure D.3.: Statistics on area A, half-axes ratio e, satellite and line number as well as mean mass m of the glue dots under variation of the cartridge-pressure $P_{\text{cartridge}}$.

E. Position per force

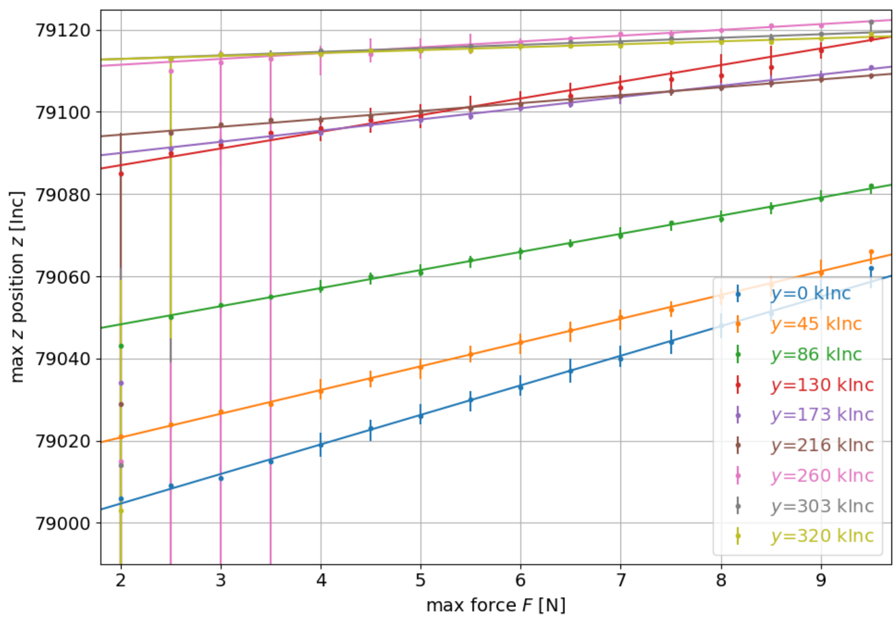

(a) Absolute position z_F with linear fits over all but the first ($F = 2\,\mathrm{N}$) data point.

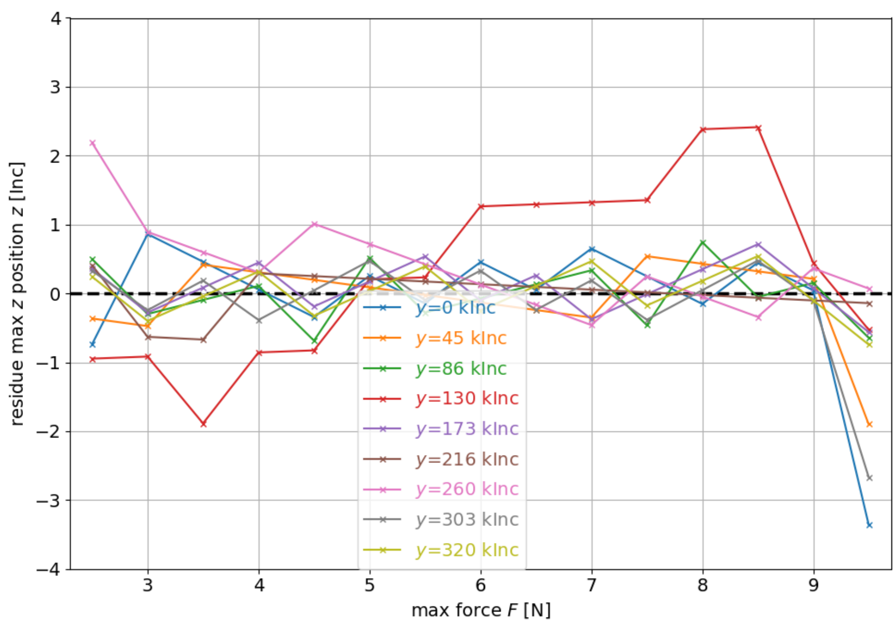

(b) Residual plot of the linear fits shown in figure E.1a.

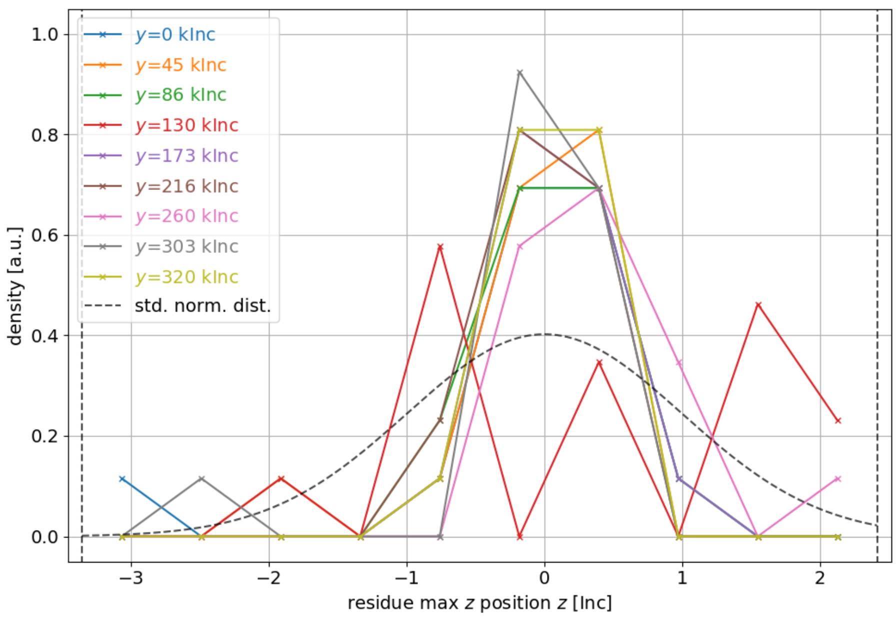

(c) Pull plot of the linear fits shown in figure E.1a.

Figure E.1.: Absolute position z_F of the z-axis while exerting force F.

The three plots above show all data - in contrast to the more readable version presented in figure 4.3. Note that there were no errorbars included into the residual as well as pull plot because of readability. The uncertainty of the residues is relatively homogeneous like the blue and green measurements already discussed in section 4.1.1. Exceptions are mentioned and discussed in section 4.1.1.
So the pull plot in figure E.1b clearly derives from figure E.1c and shows a very good coincidence between the binned pulls and the standard normal distribution, again the red measurement stands out of line.

F. Acknowledgements

I would like to thank the following people for supporting me in writing this thesis:

- Prof. Dr. Niklaus Berger for offering me this interesting topic as well as his constant support concerning any questions.
- Dr. Lars Weinstock for his constant support concerning any questions about the robot, the used software as well as review of experimental techniques.
- Peter Bernhard for constructing the robot and his constant support concerning mechanical as well as glue dispensing issues.
- Steffen Schönfelder for his support concerning 3D-printing as well as mechanical issues.
- Daniela Fetzer for carefully proofreading the thesis.
- my parents for proofreading the thesis and making my studies possible.